Multifragmentation of the remnant produced in the reaction of 1*A* GeV gold with carbon

J. A. Hauger,[1,*] P. Warren,[1,†] S. Albergo,[2] F. Bieser,[6] F. P. Brady,[3] Z. Caccia,[2] D. A. Cebra,[3] A. D. Chacon,[7,‡] J. L. Chance,[3] Y. Choi,[1,§] S. Costa,[2] J. B. Elliott,[1] M. L. Gilkes,[1] A. S. Hirsch,[1] E. L. Hjort,[1] A. Insolia,[2] M. Justice,[5] D. Keane,[5] J. C. Kintner,[3,‖] V. Lindenstruth,[4,¶] M. A. Lisa,[6,**] H. S. Matis,[6] M. McMahan,[6] C. McParland,[6] W. F. J. Müller,[4] D. L. Olson,[6] M. D. Partlan,[3,††] N. T. Porile,[1] R. Potenza,[2] G. Rai,[6] J. Rasmussen,[6] H. G. Ritter,[6] J. Romanski,[2,‡‡] J. L. Romero,[3] G. V. Russo,[2] H. Sann,[4] R. P. Scharenberg,[1] A. Scott,[5] Y. Shao,[5,§§] B. K. Srivastava,[1] T. J. M. Symons,[6] M. Tincknell,[1] C. Tuvé,[2] S. Wang,[5] H. H. Wieman,[6] T. Wienold,[6] and K. Wolf[7]

(EOS Collaboration)

[1]*Purdue University, West Lafayette, Indiana 47907*

[2]*Universitá di Catania and Istituto Nazionale di Fisica Nucleare-Sezione di Catania, I-95129 Catania, Italy*

[3]*University of California, Davis, California 95616*

[4]*GSI, D-64220 Darmstadt, Germany*

[5]*Kent State University, Kent, Ohio 44242*

[6]*Nuclear Science Division, Lawrence Berkeley National Laboratory, Berkeley, California 94720*

[7]*Texas A&M University, College Station, Texas 77843*

(Received 14 July 1997)

A high-statistics exclusive study of the multifragmentation of 1*A* GeV gold on carbon has been performed. Particles with $Z \leqslant 2$ show evidence of emission in a first prompt stage as well as in a second equilibrium stage whereas fragments with $Z \geqslant 3$ appear to be emitted essentially only in the second stage. Two methods for the separation of the $Z \leqslant 2$ particles into the two stages are given and they are in agreement. The yields for each stage are determined as a function of the event charged particle multiplicity m. The mass, nuclear charge, excitation energy per nucleon, and temperature of the remnant left after the first stage and their fluctuations have been determined as a function of m. The expansion of the remnant to fragment freeze-out is examined. The freeze-out temperature is determined from double isotope ratios as a function of m and isentropic trajectories are obtained in the temperature-density plane. The caloric curve shows a monotonic increase with excitation energy. Some of the energy is in the form of radial flow. Overall, the results are consistent with a previous statistical analysis of the data which suggests that, over a certain range of excitation energies, multifragmentation involves a continuous phase transition. [S0556-2813(98)04902-4]

PACS number(s): 25.75.−q, 21.65.+f, 25.70.Pq

I. INTRODUCTION

Multifragmentation (MF), the breakup of a nucleus into a number of fragments having a range of masses, is a characteristic response of a highly excited nucleus. Although MF has been known since the early days of cosmic ray physics [1], it has only become a subject of intense investigation since it was found to occur in high yield in high-energy proton and intermediate-energy heavy ion reactions [2]. Theoretical interest in MF followed upon the discovery that the yields of fragments with mass A_f produced in proton-xenon and proton-krypton collisions obeyed a power law $Y(A_f) \propto A_f^{-\tau}$, with $\tau \sim 2.5$ [3], as expected for a system undergoing a liquid-gas type of phase transition in the vicinity of its critical point. This result raised the possibility that MF could provide information about the equation of state of nuclear matter [4–7]. These inclusive studies also established that fragment kinetic energy spectra exhibited a strong reduction in the Coulomb barrier, suggesting fragment emission from an expanded system [8–10]. The systematics of the spectra of over 60 isotopic fragments indicated that fragments are emitted simultaneously from a common remnant, lighter in mass than the target [10]. An analysis of the relative yields of these fragments based on our thermal liquid drop model gave a freeze-out temperature of $\simeq 5$ MeV [10,11]. Fragment excitation functions for proton-nucleus interactions in the 1–20 GeV range implied that MF is a high-energy phenomenon involving excitation energies on the order of the nuclear binding energy [12,13]. The above results are particularly important because they showed that MF can be viewed as the result of a two-step process. The formation of the remnant

*Present address: Augusta State College, Augusta, GA 30910.

†Present address: Naval Research Laboratory, Washington, D.C. 20375.

‡Present address: Space Systems/Loral, Palo Alto, CA 94303-4604.

§Present address: Sung Kwun Kwan University, Suwon 440-746, Republic of Korea.

‖Present address: St. Mary's College, Morage, CA 94575.

¶Present address: Nuclear Science Division, Lawrence Berkeley National Laboratory, Berkeley, CA 94720.

**Present address: Ohio State University, Columbus, OH 43210.

††Present address: Nuclear Science Division, Lawrence Berkeley National Laboratory, Berkeley, CA 94720.

‡‡Present address: The Svedberg Laboratory, University of Uppsala, S751-21 Uppsala, Sweden.

§§Present address: Crump Institute for Biological Imaging, UCLA, Los Angeles, CA 91776.

occurs in a first step involving prompt particle emission while the breakup of the remnant involves a slower second step.

In recent years, further progress has been made possible by exclusive studies of MF, in which practically all the fragments emitted in a given event are detected. The ALADIN Collaboration studied the MF of (400–1000)A MeV xenon, gold, and uranium nuclei incident on targets ranging from Be to U [14,15]. Fragment yields were found to be independent of the entrance channel when scaled for projectile size, suggesting that MF occurred following equilibration. Similar universal scaling was observed by Beaulieu *et al.* [16], again pointing to the thermal nature of MF. The EOS Collaboration studied the MF of 1A GeV gold on carbon and analyzed the distribution of projectile fragments by applying the methods used in the study of critical phenomena. Four critical exponents were obtained from the data [17,18]. The values of these exponents were found to be consistent with those of the Ising (liquid-gas) universality class, suggesting that, over a certain range of excitation energies, MF can be understood as arising from a continuous phase transition similar to that involving ordinary fluids. Along with the earlier inclusive studies, these experiments suggested that following its formation in a prompt preequilibrium step, the remnant undergoes equilibration prior to its breakup.

The above experiments indicate that thermodynamic or statistical interpretations of MF [19,20] should be appropriate. Statistical models are indeed able to account for many features of the data [21]. However, it is clear that dynamical effects must also play an important role. The occurrence of the preequilibrium process can be followed by means of various dynamical codes [22,23]. The resulting remnant can be characterized by a few global variables, such as nuclear charge, mass, excitation energy, and temperature. These variables may depend on the centrality of the collision [24] as measured, for example, by the event charged particle multiplicity m. The properties of the remnant are of great importance to an understanding of MF since the nature of this process will vary with its excitation energy per nucleon, E^*/A. Within the context of a phase transition picture, MF will first occur at moderate excitation energies from the liquid state, resulting in the emission of light particles and fragments and the formation of a heavy residue. At a higher E^*/A, the system passes through the critical region and fragments are emitted with a broad range of masses according to the power law. At still higher E^*/A the system undergoes vaporization, disassembling into nucleons and light particles.

This paper deals with the dynamics of the MF of 1A GeV gold (beam rapidity $y=1.35$) plus carbon and the characterization of the remnant that eventually undergoes MF. Section II presents the details of the experiment and data analysis. Section III deals with the separation of the prompt preequilibrium particles and Sec. IV presents the properties of the remnant. Section V deals with the expansion of the remnant towards fragment freeze-out. Finally, a summary of the results is given in Sec. VI. Some of our results have been published previously [25,26].

II. EXPERIMENTAL DETAILS

A. EOS detector

A beam of high-energy gold ions from the LBL Bevalac was incident on the target and detector configuration shown in Fig. 1. The experiment used four major detector systems to track and detect fragments produced in the nuclear collisions: the EOS time projection chamber (TPC), a multiple sampling ionization chamber (MUSIC II), a time-of-flight wall, and a neutron spectrometer (MUFFINS). Only the first two of these detectors were used in the present analysis.

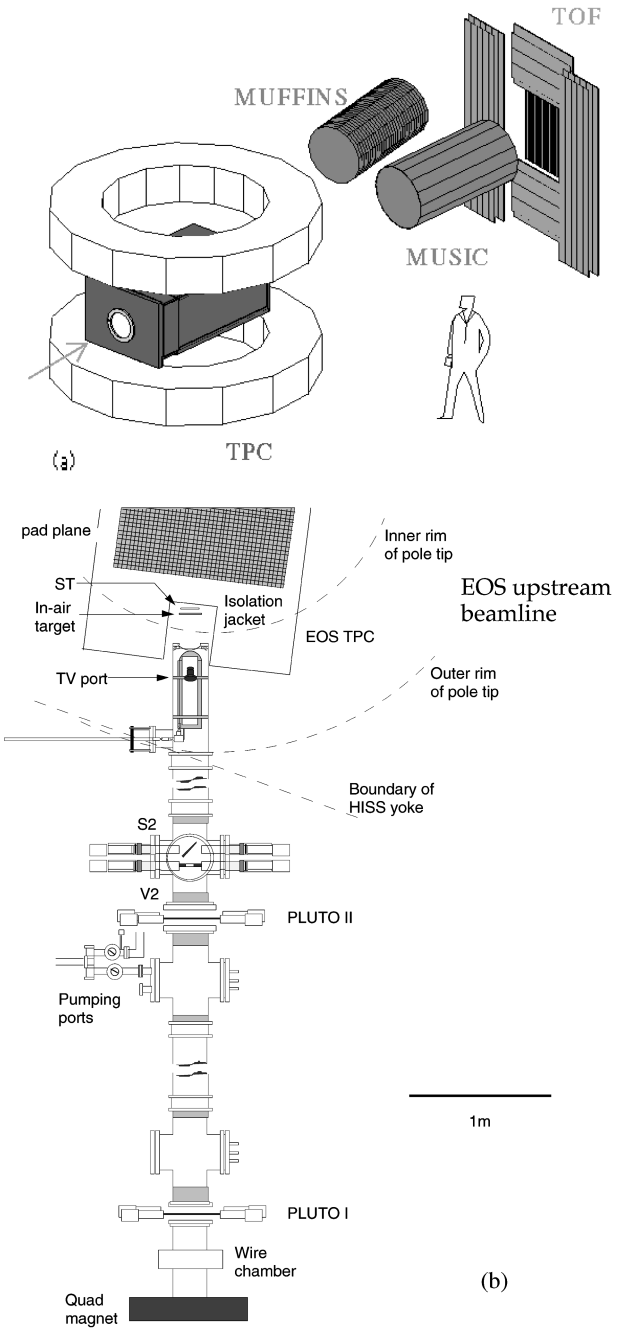

FIG. 1. The EOS detector: (a) main components, (b) plan view of upstream beam line detectors. S_1 and V_1 are upstream of the quadrupole magnet and are not shown.

An evacuated beam line, shown in Fig. 1, led to the TPC. It contained several beam defining detectors. Two thin (100 μm) plastic scintillator signal-veto detectors ensured proper beam alignment and prevented beam interactions occurring outside the target from being recorded. They also provided beam intensity and arrival time information. To trigger the downstream detectors to read an event, the beam was re-

quired to pass through both veto (V1,V2) scintillator holes, 3.2 cm in diameter, and hit the signal (S1,S2) detectors.

Between the signal-veto detectors were the PLUTO detectors located 2 m apart in air gaps along the beam line. The PLUTO detectors determined the incident beam direction for each event. Scintillator and optical fibers arranged in a grid at 1 cm intervals and four photomultiplier tubes attached to the edges of the scintillator provided vertical and horizontal beam position. An incident beam vector for each event was constructed by combining these vertical and horizontal positions at the planes of the two PLUTO detectors. The angular resolution of these detectors was 1.2 mrad and 0.5 mrad in the horizontal and vertical planes, respectively. Since the target is located in the field of the dipole magnet housing the TPC, some bending of the beam in the fringe field occurs prior to the interaction with the target. A small average correction to the PLUTO beam vector was made to account for this effect.

The beam line was followed by a 490 mg/cm^2 carbon target located in air just upstream of the TPC and 3 cm in front of the trigger scintillator (ST). Events in which large energy losses occurred in this detector were vetoed. The minimum bias trigger formed in this manner eliminated the bulk of the noninteracting beam as well as some of the most peripheral interactions.

The TPC [27] detected, identified, and tracked fragments with charges in the range $1 \leqslant Z \leqslant 8$, providing a nearly 4π solid angle coverage in the center-of-mass system. Three-dimensional tracking and charged particle identification permitted momentum and energy reconstruction of these fragments. The entire TPC volume was situated between the poles of the Heavy Ion Superconducting Spectrometer (HISS) dipole magnet and was rotated 7° with respect to the beam line to optimize coverage of charged fragments bending in the 1.3 T magnetic field. The TPC has an active drift volume 154 cm in the beam (z) direction, 96 cm wide in the bending (x) direction, and 75 cm high in the drift (y) direction. Electrons drifted at about 5 cm/μs in the parallel electric and magnetic fields to the floor of the TPC, which was tiled with 15 360 pads. The pad array provided a two-dimensional horizontal location of the track and the 256 samplings of the drift time gave the vertical location. The TPC thus provided over 2×10^6 pixels for tracking. The dE/dx was measured with an analog system. A laser calibration system was used to monitor the electron drift velocity and to map the distortions in the electron drift path.

MUSIC II [28] detected and tracked fragments with charges $8 \leqslant Z \leqslant Z_{\text{beam}}$. The detector consisted of a cylindrical vessel filled with P10 gas slightly above atmospheric pressure. The ends of the vessel were enclosed by low-mass kapton windows to minimize multiple scattering. The inner diameter of the vessel was 124 cm with a length of 250 cm. Three field cages with active areas of 102.4 cm by 60 cm and a depth of 51.2 cm each were aligned in the vessel. Each anode plane was composed of 16 anode strips 3 cm wide. The two field cages at the ends of the vessel generated horizontal drift fields while the central field cage produced a vertical drift field.

The MUSIC II chamber operated without gas gain and so was capable of detecting the heavier, more highly ionizing charged fragments without electronic saturation. A track liberated about $70Z^2$ ion pairs per cm, which were used to determine the charge of each fragment. The electrons drifted at roughly constant velocity through the active volume and arrived at the anode with a time delay proportional to their initial distance from the anode plane. The anode strips measured the drift times, which provided information about the position and slope of the fragment's path through the cage. Track segments in the three cages with matched charge, slope, and position were combined to reconstruct the fragment tracks with ~95% efficiency.

B. Data reduction

1. TPC

The TPC data analysis translates the three-dimensional electronic signals into space points and calculates the amount of ionization associated with each hit. Pad signals were analyzed for drift time measured in 100 ns time pixels. Peaks in the analog-to-digital converter (ADC) spectrum were found by searching for three or more adjacent pixels with the central pixel being the highest. The peak height is found after fitting these ADC readings with a Gaussian. A correction for electron diffusion in the vertical direction during the drift to the pad plane was applied. A deconvolution procedure was applied for overlapping peaks.

The pattern recognition routine [29] first examined the pad rows most downstream from the target. If three hit clusters contained colinear hits, an initial track segment was fit. A straight line projection was used to search for a hit cluster on the next pad row upstream. If at least two more hit clusters were found, a helix was fit and extrapolated to the next pad row. The helix was updated if another hit cluster was found and the procedure repeated until no further hit clusters were found. The radius of the helix fit to each track and the magnetic field map were used to calculate the rigidity of the fragment. The momentum was obtained after charge identification. Track segments were then merged and a vertex with a resolution of 0.4 cm was reconstructed. The vertex provided a starting point to reevaluate track fits and allowed elimination of tracks coming from interactions outside the target. Tracks fit using the vertex information showed improved rigidity and momentum precision over tracks fit by simply merging segments. Typically, a track was constructed from ~100 hits.

The energy loss of the fragment, dE/dx, was obtained from the sum of the amplitudes of all time pixels associated with the track. Landau fluctuations were smoothed by including only the lowest 80% of samples of energy loss for each track. Figure 2 shows the 80% truncated mean of dE/dx versus rigidity for charged particles detected in the 1A GeV Au+C collisions. Note that charge bands are generally well separated. Isotope separation was possible up to $Z=4$ and was made by graphically scribing boundaries along valleys in the contour plot of the distribution. While good separation was achieved at rigidities corresponding to the rapidity of the projectile remnant, where the particle yields peak, the separation is not as good for particles having low rigidity. For example, the yield of ^{4}He is cut off at a rigidity of 1.6 GeV/c and some of the ^{3}He yield at lower rigidities may actually represent ^{4}He. The separation in rigidity between ^{1}H, ^{2}H,

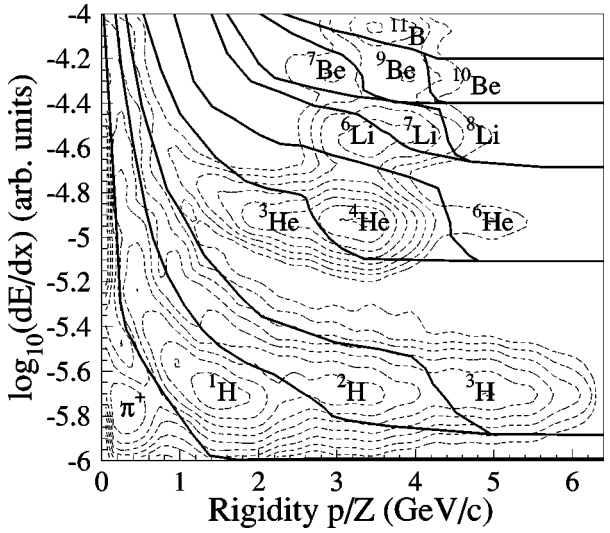

FIG. 2. Contour plot of dE/dx vs rigidity in the TPC for 1A GeV Au+C. Adjacent contours correspond to a factor-of-2 difference in the number of particles.

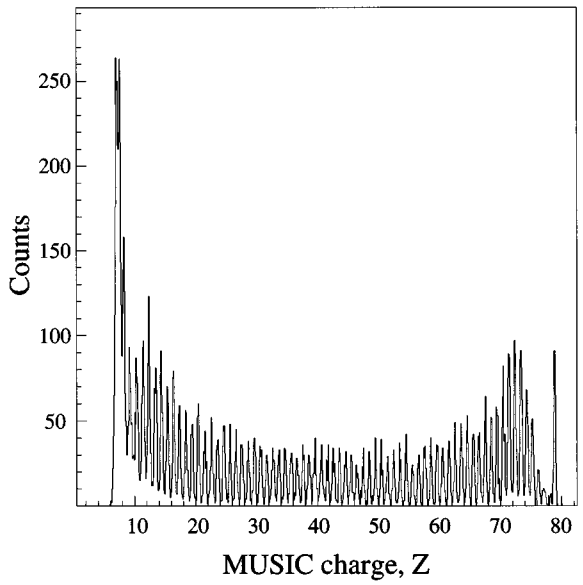

FIG. 3. Charge resolution of MUSIC II.

and ^{3}H is better than that between He isotopes and isotopic misassignment is not a problem for $Z=1$ particles.

2. MUSIC II

Pulse shapes from gold beam particles were used to extract the amplitude and position of hits from each anode strip. Overlapping hits were deconvoluted and track segments constructed in each field cage from the calculated set of amplitudes and positions of the 14 interior anode strips in each cage. The angle or slope of each track segment relative to the anode plane was also computed. Combining vertical and horizontal cages produced a position in space at the detector midpoint and an associated three-dimensional track vector. Track segment vectors from all cages were projected onto a single plane perpendicular to the main axis of the detector. Tracks were then reconstructed by requiring matches in charge between track segments in the three cages and matches in slopes and projected positions between track segments in the horizontal drift cages.

Peaks in the charge distribution were visually identified and corrected to coincide with an integer charge. The maximum charge peak was set to be that of the gold beam, 79. Although greatly ($>99\%$) suppressed by the trigger, enough beam particles were detected to give a clearly identifiable peak. An example of the charge resolution ($\sim 0.2Z$) of the reconstructed tracks in MUSIC II is shown in Fig. 3. The peaks corresponding to the various fragments are well resolved and the charges were assigned by stepping down from 79.

C. Event reconstruction

The experiment produced a high-statistics (1.2×10^5) set of minimum bias events. A wide range of total event multiplicities was detected. The charged particle multiplicity distribution of fully reconstructed events is displayed in Fig. 4. While the distribution peaks for events with low multiplicities, $m\sim4$, it extends to ~60, corresponding to a nearly complete breakup of the gold nucleus.

Figure 5 shows the distribution of the total reconstructed charge of each event. The data peak near the charge of gold but extend to much smaller total charges. The causes of this low-charge tail include losses due to inefficient track reconstruction [30] as well as a reduction in TPC efficiency whenever a highly charged fragment is emitted. This effect is discussed in detail below. The shaded region indicates the events with a reconstructed charge of 75–82, selected for further analysis. Approximately 4×10^4 events met this criterion. If all charges from the gold projectile and carbon target were collected in each event, the reconstructed charge would be $79+6=85$. However, a GEANT simulation shows that fragments from the carbon target are not likely to enter the TPC volume in the low-multiplicity events [30], and so the total reconstructed charge in the data is expected to be about 79 in these events. At high multiplicity, the simulation also shows that some tracks in the TPC are missed or lost

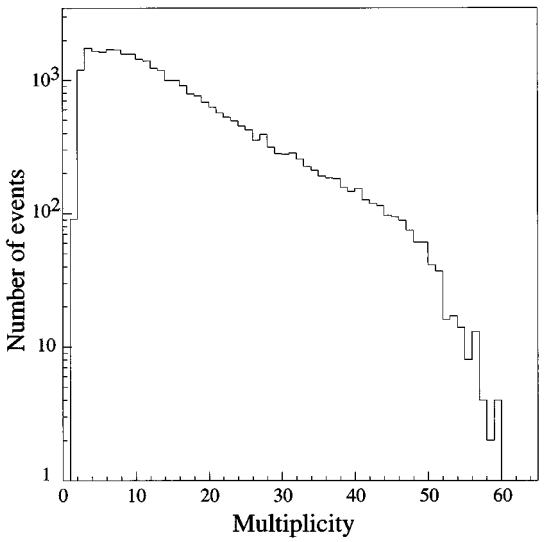

FIG. 4. Charged particle multiplicity (m) distribution for fully reconstructed events in 1A GeV Au+C interactions. Fission events have been suppressed.

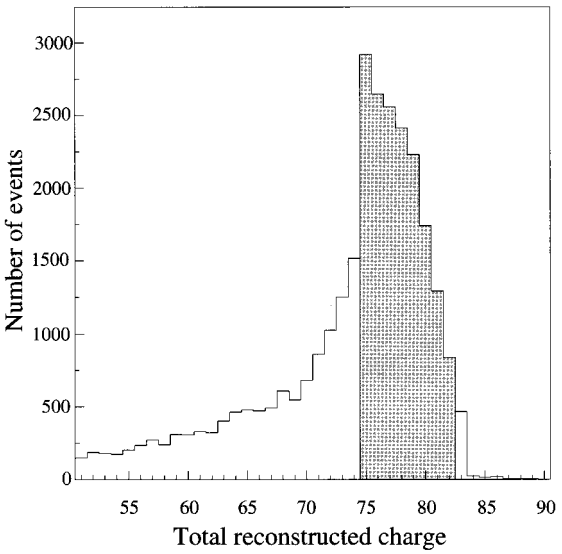

FIG. 5. Distribution of the total reconstructed charge in each event. The shaded region marks the events selected for further analysis.

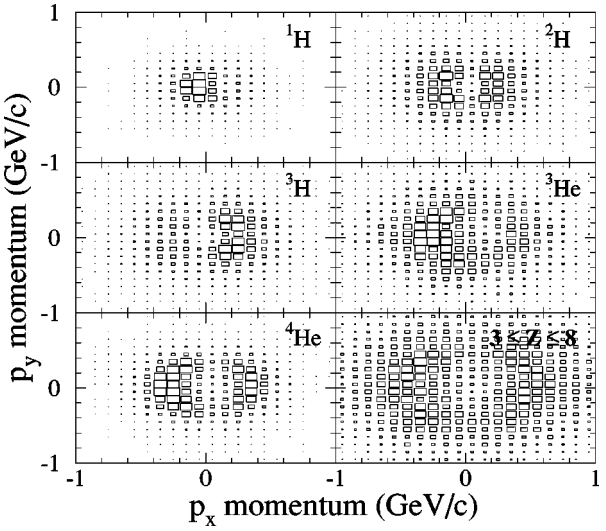

FIG. 7. Light particle and fragment yields in the TPC as a function of transverse momentum components, where y designates the vertical direction and x the horizontal direction. The size of the rectangles is proportional to the number of particles.

due to two-track resolution limitations, and so the data are expected to have a total charge of about 79 in the high-multiplicity events as well. This expectation is borne out by the data, which show essentially constant reconstructed charge at all m. See Fig. 6.

In reverse kinematics, most reaction products continue to move at near beam rapidity through the detector systems so that most tracks in the TPC are found in a cone centered about the beam path. The heavy fragments are not detected by the TPC but leave saturated ionization trails. This cloud of liberated electrons reaches the pad plane in the detector along with the ionization from the lighter particles, which the TPC does detect. Light fragments with low transverse momentum p_t traveling at near beam rapidity and having a mass-to-charge ratio (M/Z) similar to that of the beam will have only a small separation from the track of a heavy fragment when exiting the chamber. If this separation is smaller than the two-track resolution of the detector ($\sim$2.5 cm), it is likely that the ionization of the light fragment will be merged with that of the heavy fragment. Because the size of the largest fragment decreases at high multiplicity, the inefficiency of the detector caused by the large fragment will be less severe in the highest-multiplicity events. On the other hand, at high multiplicity we expect more severe losses due to two-track resolution especially for low-p_t particles [30].

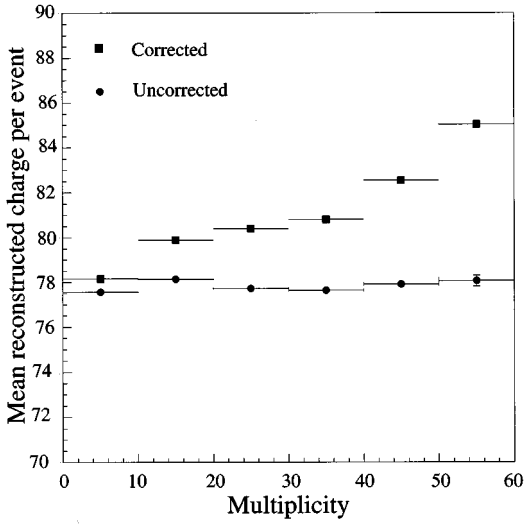

FIG. 6. Dependence of total reconstructed charge on multiplicity. The results apply to the shaded events in Fig. 5.

The heavy fragments will typically have $M/Z\sim2.2$ (see Fig. 11). Therefore ^{2}H and ^{4}He will tend to follow the path of the large fragment through the detector. However, protons will have a smaller radius of curvature than the heavy fragment. We therefore expect protons with a zero or negative momentum component p_x, which are farthest from the large fragment track, to be virtually unaffected by it. On the other hand, protons with $p_x>0$ may have a reduced detection efficiency. The inefficiencies should be largest for particles moving in the plane of the beam, i.e., with $p_y\sim0$.

The above effects are evident in plots of the p_y versus p_x distribution of particles detected in the TPC, displayed in Fig. 7. Focusing first on the protons, we note that the distribution is asymmetric, with more protons having $p_x<0$ than $p_x>0$. If we assume that the distribution of protons with $p_x<0$ is unaffected by the reduced detector efficiency, then comparing the yield of protons with $p_x<0$ to the number with $p_x>0$ gives an estimate of the detector efficiency for protons. These average values of the efficiency can then be used to correct the total reconstructed charge as a function of m and are listed in Table I for various multiplicity bins.

The impact of the ionization trail of the heavy fragment on the light fragment detection efficiency is also evident in plots of p_y versus p_x for the other hydrogen and helium isotopes. The main effect is that all these particles have an efficiency ''hole'' in the middle of the distribution. Therefore we could not assume, as in the case of the protons, that one-half of the distribution was unaffected. Instead, we made an estimate of the number and average kinetic energy of the

TABLE I. Light fragment efficiency estimate for the TPC as a function of multiplicity.

Multiplicity bin	^{1}H	^{2}H	^{3}H	^{3}He	^{4}He
1–10	88.5	86.7	81.3	84.1	86.3
11–20	92.2	88.4	82.9	82.3	85.2
21–30	92.6	90.2	84.6	88.0	86.5
31–40	93.6	92.3	88.5	91.6	87.9
41–50	91.8	92.0	93.7	89.0	87.5
51–60	90.5	94.9			78.3

lost particles by fitting a two-dimensional function of the form

$$f(p_t)=\frac{N}{\{1+\exp[(p_t^A-B)/C]\}} \tag{1}$$

to these p_x and p_y distributions in various multiplicity intervals. Here, A, B, C, and N are fit parameters and p_t is the transverse momentum. Fits were performed for ^{3}H and ^{3}He by combining the two highest-multiplicity bins. The results are summarized in Table I.

Figure 7 shows that $Z=3$–8 fragments also suffer from reduced efficiency in the middle of the distribution. However, the total reconstructed charge does not require an efficiency correction due to the loss of these fragments because the charge cut shown in Fig. 5 effectively eliminates events with undetected fragments in this charge range. The mean transverse kinetic energies of $Z=3$–7 fragments are discussed in Sec. V E. The reduced TPC efficiency primarily affects these energies via the width of the momentum distribution. The reduced efficiency for $p_x\sim 0$ makes the width of the p_x distribution, σ_{p_x}, too large. However, the width of the p_y distribution, σ_{p_y}, is essentially unaffected. Therefore the ratio of widths, $2\sigma_{p_y}^2/\sigma_{p_x}^2+\sigma_{p_y}^2$, was applied as a multiplicity-dependent correction factor. The effect of this correction is to reduce the mean transverse energy of the fragments, thereby correcting for the preferential loss of low-p_x fragments. The correction amounted to $\sim 30\%$, on average, for small m, but to only $\sim 2\%$, on average, for large m.

Since the pool of events used in the present analysis is known to have a total charge peak at 78, we have likely selected events which have missing fragments. Therefore the efficiency values listed in Table I are worst case estimates for the efficiencies of all particles produced in the event including the prompt component.

The total reconstructed charge was corrected for efficiency by determining the mean number of light particles of each type in each event as a function of m. These yields were then corrected by dividing by the TPC efficiency corresponding to the multiplicity bin and particle being considered. The amount of additional charge associated with these ''missing'' particles was then added as a correction to the average reconstructed charge. The mean corrected and uncorrected reconstructed charges per event are compared in Fig. 6. The corrected total reconstructed charge increases monotonically with event centrality from ~ 78 to ~ 85 as expected. This increase occurs even though the efficiencies are slowly improving because the number of particles being corrected is larger at high multiplicity. Reconstructing a total charge via simulation also suggests that the efficiencies listed in Table I describe the fraction of missing particles well.

III. SEPARATION OF REACTION STAGES

In this section we describe the procedure used to separate the particles emitted in the first step from those associated with the decay of the remnant. We begin by presenting evidence for the occurrence of two reaction stages. Next, we determine the velocity of the remnant in the laboratory frame and show how this velocity can be used in conjunction with the transverse momenta of heavy fragments to determine their average mass for a given charge. We then transform the measured energy spectra to the moving frame and describe two methods of separating the two stages. Our analysis supports the results mentioned in the Introduction, which indicated that a first prompt preequilibrium step is followed by a second step in which the equilibrated remnant breaks up.

A. Evidence for two reaction stages

An indication that protons are emitted in two distinct reaction steps can be seen in a contour plot of the transverse momentum p_t versus laboratory rapidity y, Fig. 8. We note a strong component centered near $y_{\rm beam}$ and at low p_t, with a

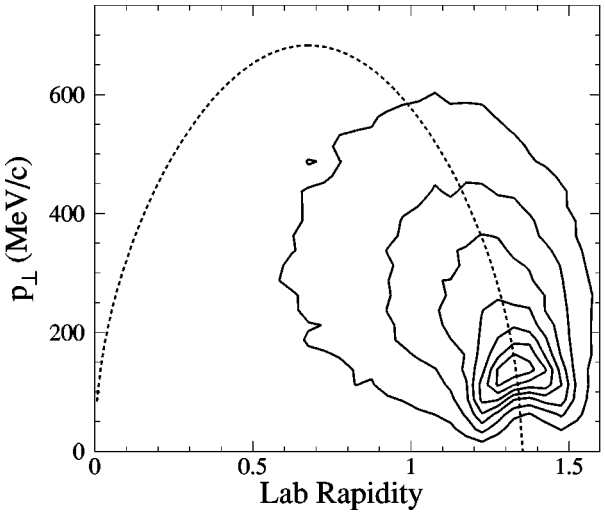

FIG. 8. Linear contours of transverse momentum of protons versus laboratory rapidity. The contours cover a factor-of-10 range in proton number. The dashed curve corresponds to quasielastic nucleon-nucleon scattering.

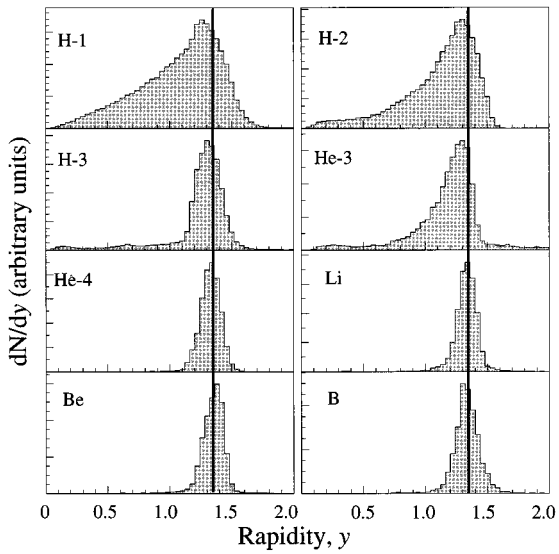

FIG. 9. Laboratory rapidity distributions of light particles and fragments. The heavy lines correspond to y_{beam}.

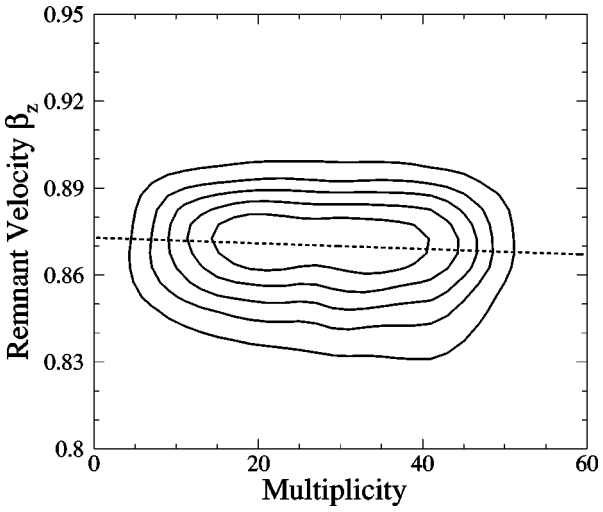

FIG. 10. Remnant source velocity contours as a function of m. The dashed line is the resulting average β_z.

second distribution extending to lower rapidity and high p_t. The first component is suggestive of thermal emission from the remnant in a second reaction step. In reverse kinematics, the excited remnant moves at nearly beam rapidity in the laboratory reference frame. Consequently, the rapidity distribution is expected to be centered near y_{beam} for protons and fragments emitted from the projectile remnant. Further, if the remnant is at thermal equilibrium, the emitted protons will have low p_t.

The second component is indicative of prompt emission in a first stage involving elastic and inelastic nucleon-nucleon collisions. The dashed curve, which follows the contour ridges, represents quasielastic scattering of a nucleon in the projectile with a nucleon in the target. This curve is broadened by the initial Fermi motion of the nucleons in the projectile and target nuclei [31]. By adding an inelastic component, many of the features of the data are qualitatively reproduced. In the elastic scattering case, the distribution starts at y_{beam} for low transverse momentum. This corresponds to a glancing nucleon-nucleon collision. The curve extends to lower rapidity for higher p_t, reflecting higher-momentum transfer collisions between the interacting nucleons. Further confirmation of the nature of this first step is given by intranuclear cascade calculations, which represent the first step of the interaction as a series of quasifree nucleon-nucleon collisions. Thus, the cascade code ISABEL [23] yields a plot of p_t vs y for 1A GeV Au plus C that closely resembles the experimental contours observed for the second component.

The above features can also be seen in Fig. 9, which shows the laboratory rapidity distributions of particles and light fragments detected in the TPC. The proton distribution shows a Gaussian peak centered near y_{beam} and a tail extending to low rapidities. The peak near y_{beam} includes the first component in Fig. 8 and therefore represents second stage protons (as well as some first stage protons). The tail at low y corresponds to the second component in Fig. 8 and thus indicates the emission of prompt protons. The distributions for ^{2}H, ^{3}H, ^{3}He, and, to a lesser extent, ^{4}He exhibit similar features. In contrast, the distribution for fragments heavier than helium is symmetric about y_{beam}, implying that these fragments are emitted virtually only from the decaying remnant in the second step of the reaction. Because of the previously mentioned uncertainties in particle identification at small rigidities we estimate that $\lesssim 10\%$ of the ^{3}He yield for $y \leqslant 1.0$ may actually belong to ^{4}He. However, the effect on the ^{4}He spectrum in Fig. 9 would not be noticeable because the yield of ^{4}He is an order of magnitude larger than that of ^{3}He.

It might appear that a straightforward separation of prompt protons could be performed by reflecting the forward half of the rapidity distribution. However, such a procedure is not valid since, as noted in Fig. 8, there is a strong component of prompt protons near beam rapidity, but with a large transverse momentum.

B. Remnant source velocity and heavy fragment masses

In order to separate the two reaction stages it is first necessary to determine the velocity of the moving remnant, β_z. In a simultaneous thermal breakup of the remnant, particles are emitted isotropically in the moving source frame and their laboratory velocities may be used to calculate β_z. The moving reference frame is computed from the mass-weighted average of the fragment velocities for each event [32]. Therefore,

$$\langle \beta_z \rangle = \frac{\Sigma m_i \gamma_i \beta_{z_i}}{\Sigma m_i \gamma_i}, \tag{2}$$

where m_i is the fragment mass and β_{z_i} is the velocity of the fragment in the laboratory frame. Only those fragments with good mass identification and no prompt component are used in the source velocity calculation, i.e., Li and Be. A least squares fit of the source velocity as a function of m yields $\langle \beta_z \rangle = 0.873$ for $m = 0$, decreasing to $\langle \beta_z \rangle = 0.867$ for $m = 60$. The fit is shown in Fig. 10. Other combinations of isotopes were tested to check the sensitivity of the calculation. The resulting least squares fits differ by less than 0.5%. In any particular event only one or two of these fragments

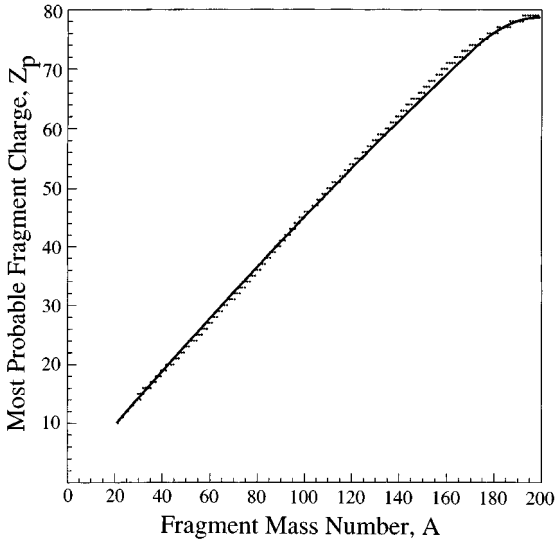

FIG. 11. Average masses of heavy fragments with charges determined with MUSIC II. The solid line is the EPAX parametrization [33].

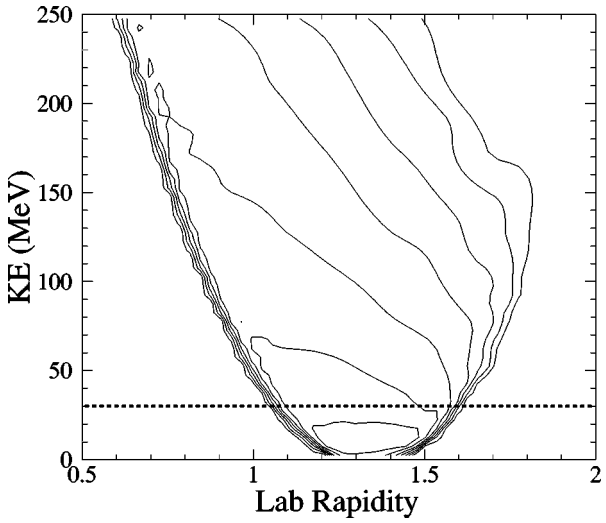

FIG. 12. Logarithmic contour plot of proton kinetic energy in moving system vs laboratory rapidity. Adjacent contours correspond to a factor of 2.4 difference in proton number. The horizontal line at 30 MeV divides the two reaction stages.

are found and so there are fluctuations in the calculated source velocity, event to event. However, isotropic emission of these fragments ensures that the correct average velocity as a function of m is determined. The source velocity from the fit was used to transform particle velocities for a given multiplicity.

The fractional mass difference of fragments with $Z \geqslant 6$ is too small to permit a mass determination in the TPC. It is possible, however, to use the above values of $\langle \beta_z \rangle$ to infer average heavy fragment masses. In turn, comparison of these masses with those obtained in other experiments confirms the validity of $\langle \beta_z \rangle$. Our procedure is based on the fact that heavy fragments are emitted isotropically from the decaying projectile remnant and, on average, will be moving with the same velocity in the laboratory reference frame as this remnant. Consequently, an estimate of the mass of these fragments is possible using the TPC momentum information in conjunction with the above values of $\langle \beta_z \rangle$. The mass estimate proceeds by approximating, for each fragment, the total laboratory energy $E_{\mathrm{tot}} = \gamma M = p_z / \langle \beta_z \rangle$. We ignore the transverse momentum since $p_z \gg p_t$. Average masses of $Z = 6$–8 fragments obtained in this way are in close agreement ($\sim 1\%$) with those measured in target fragmentation of xenon and krypton by high-energy protons [3,10].

Mass estimates for the heavy fragments detected in the MUSIC II detector were made in the same way as described above. The measured charge of the heavy fragments is plotted versus the estimated mass in Fig. 11. The results agree well with the EPAX parametrization of the most probable charges of products of high-energy reactions [33].

C. Separation by constant velocity cut

In order to separate the two reaction steps the kinetic energy of each fragment was first transformed to the reference frame of the moving projectile remnant. In Fig. 12 the proton kinetic energy (KE) in the moving system is plotted versus the laboratory rapidity. The higher-energy protons are found preferentially at lower rapidity than the remnant source. We note that above KE$\sim$30 MeV, the distribution becomes asymmetric due to the increased prompt component at low rapidity. At lower kinetic energies, the distribution appears roughly symmetric about y_{beam}. Similar plots for the other $Z = 1$ and $Z = 2$ particles also show that the distributions become asymmetric when the kinetic energy per nucleon increases above $\sim$30 MeV/nucleon. This value of kinetic energy per nucleon is common to all of the light fragments having a strong prompt component. Furthermore, the kinetic energy spectra show a distinct kink at this energy per nucleon (see Fig. 13). Therefore, cuts made at 30 MeV/nucleon are used to approximately separate the two components. Adjustments of ± 5 MeV/nucleon in the location of this cut have only a small effect on our subsequent results.

Since the kinetic energy of each particle is computed by transforming to the moving remnant reference frame, we checked the sensitivity of the spectra to the value of the

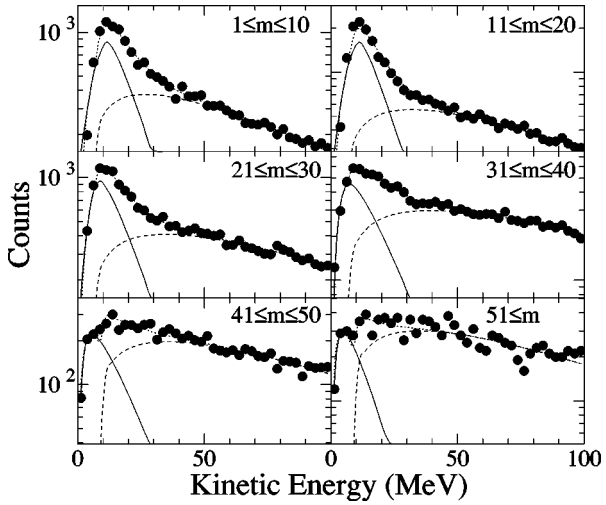

FIG. 13. Two-stage fit to the proton kinetic energy spectrum for indicated multiplicity intervals. Dashed curve, first stage; solid curve, second stage; dotted curve, sum of two stages.

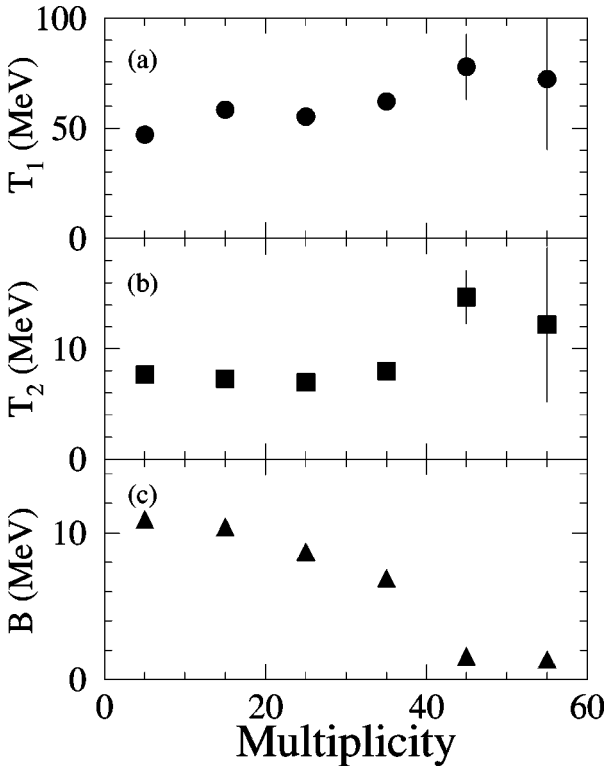

FIG. 14. Multiplicity dependence of the parameters in the two-stage fit to the proton spectra.

moving frame's laboratory velocity. After varying the projectile remnant reference frame by 1%, the spectra differ only slightly in the lowest-energy bins, implying that the systematic error in the kinetic energy spectra due to the moving reference frame is insignificant.

D. Separation by deconvolution of spectra

The procedure for the separation of the two reaction stages outlined in the preceding section is an oversimplification because it ignores the continuous nature of particle spectra. In this section we separate the first and second stage protons by assuming that the second stage source is in thermal equilibrium. The proton KE spectrum can then be characterized by a Maxwell-Boltzmann (MB) distribution for low KE (second stage) and a simple empirical parametrization of the high-KE tail (first stage). For the composite light particles, a coalescence analysis provides the first stage contribution to the spectra. Subtraction from the experimental spectra, which were corrected for the reduced TPC efficiency by means of Eq. (1), then yields the second stage spectra.

1. Protons

For all but the highest-multiplicity events, the proton kinetic energy spectra in the remnant frame show a distinct kink at about 30 MeV. The spectral shapes both above and below 30 MeV appear similar to negative exponentials, but with distinctly different slopes. Protons emitted from a thermalized equilibrium source would follow the MB distribution, which is approximately a negative exponential for large kinetic energy. This suggests fitting the proton kinetic energy spectra with two MB-like functions, one for each of the reaction stages. With this procedure, the proton spectra can be deconvoluted into first and second stages in a continuous way, and thermal parameters such as the second stage temperature and Coulomb barrier can be extracted.

The MB function of kinetic energy E with Coulomb barrier B is

$$f_{\mathrm{MB}}(E,B,T)=(E-B)^{1/2}\exp[-(E-B)/T] \quad \text{for } E\geqslant B$$
$$=0 \quad \text{for } E<B. \tag{3}$$

The Coulomb barrier B should be averaged (or smeared) for at least three reasons: (1) The remnant nucleus loses charge and expands (both of which decrease the barrier $B=Ze^2/r$), (2) the source velocity is only an average, and the source in individual events is really moving with respect to KE=0, allowing KE$<B$ in the average frame, and (3) there may be a radial position dependence according to fragment charge. The MB functions were modified with a smeared Coulomb barrier, by averaging $f_{\mathrm{MB}}(E,B,T)$ over a range of barriers from B_1 to B_2 as follows:

$$g_{MB}(E,B_1,B_2,T)=\frac{1}{B_2-B_1}\int_{B_1}^{B_2}dB(E-B)^{1/2}\times\exp[-(E-B)/T]$$
$$=\frac{1}{B_2-B_1}T^{3/2}\left\{P\left[\frac{3}{2},\frac{(E-B_1)}{T}\right]-P\left[\frac{3}{2},\frac{(E-B_2)}{T}\right]\right\}, \tag{4}$$

where $P(a,x)$ is the incomplete gamma function.

For the first stage, the Coulomb barrier of Au+C ($Z=85$) is over 17 MeV. Because the second stage remnant charge decreases to $\sim Z_{\mathrm{Au}}/2$ in high-multiplicity events (see Sec. IV A), the first stage Coulomb barrier was averaged from $B_1=8.5$ to $B_2=17$ MeV. For the second stage, the barrier was averaged from $B_1=0$ to $B_2=B$, where B is a fit parameter.

In all of the following analyses, the data were divided into six event multiplicity intervals. Only protons with $p_x\leqslant 0$ were used, to avoid the TPC two-track resolution inefficiency for protons with positive p_x (Sec. II C). The spectra were fitted from 0 to 100 MeV in KE with the sum of two g_{MB} functions:

$$N_1 g_{\mathrm{MB}}(E,8.5\ \mathrm{MeV},17\ \mathrm{MeV},T_1)+N_2 g_{\mathrm{MB}}(E,0,B,T_2). \tag{5}$$

There are five parameters in this fit: N_1 and N_2 are the first and second stage normalizations, T_1 is the stage one slope parameter, T_2 is the second stage temperature, and B is the maximum second stage effective Coulomb barrier. A good fit to the proton KE spectra is obtained for all six multiplicity intervals, as seen in Fig. 13. Plots of T_1, T_2, and B vs multiplicity are shown in Fig. 14. The values of T_1 are comparable to the first stage slope parameters obtained in other high-energy experiments [34]. T_2 increases with m to a comparable extent as the second stage initial and final temperatures that were estimated by other techniques, as described in Secs. IV C and V A. Since all these techniques assume

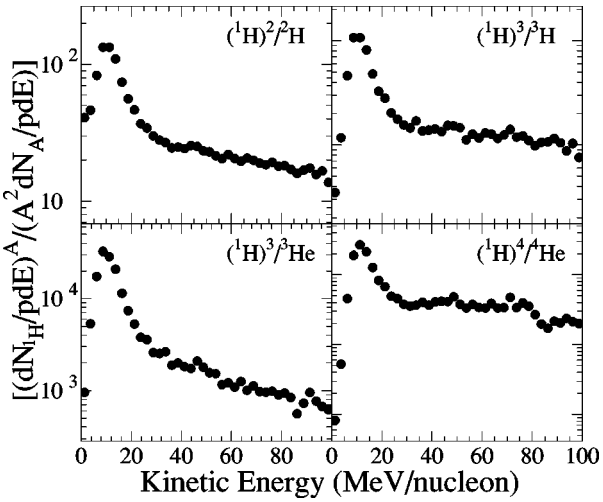

FIG. 15. Coalescence ratio of light particles as a function of kinetic energy per nucleon.

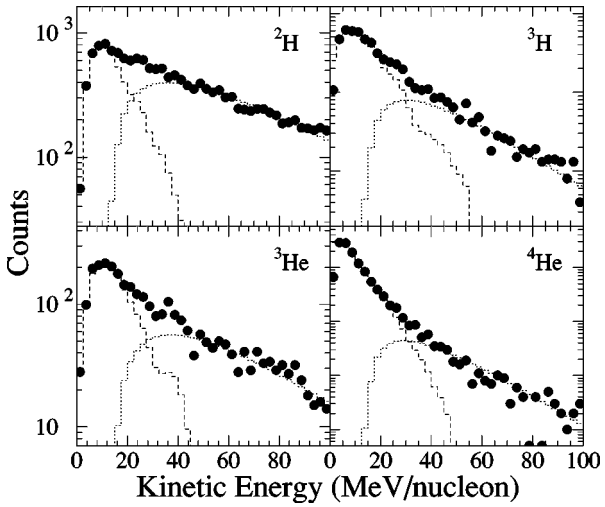

FIG. 16. Decomposition of the KE/n spectra of composite $Z=1$ and $Z=2$ particles into two reaction stages for the $21 \leqslant m \leqslant 30$ multiplicity interval. Dotted histogram, first stage; dashed histogram, second stage.

equilibration and give consistent and reasonable temperatures, the results support the validity of this assumption. The decrease of B with increasing m reflects the corresponding decrease in the density of the remnant (Sec. V D). The above procedure effectively decomposes the protons into a prompt first stage and an equilibrium second stage with no arbitrary KE cut.

2. Composite particles

The emission of prompt composite particles is generally believed to involve coalescence of scattered protons and neutrons in the first stage of the reaction [35]. Gutbrod *et al.* [36] have given an expression for the three-dimensional phase space density of a light cluster of mass A relative to that of protons. Because of our limited statistics, it is convenient to integrate over angles, which gives the one-dimensional phase space density ratio

$$\frac{[dN_{\text{proton}}/pd\text{KE}]^A}{[A^2dN_A/pd\text{KE}]} = \text{const} \times \left(\int f^A_{\text{proton}}(E,\Omega)d\Omega \right)^{-1}, \tag{6}$$

where $f_{\text{proton}}(E,\Omega) = N_{\text{proton}}(E,\Omega)/N_{\text{proton}}(E)$. Note that the integral on the right side of Eq. (6) is equal to unity for $A=1$ by construction. However, this integral will differ from unity for $A>1$ if $f_{\text{proton}}(E,\Omega)$ varies with Ω, i.e., if the proton angular distribution varies with energy.

Figure 15 shows the coalescence ratios of Eq. (6) for $Z=1$ and 2 particles. The ratios show a large peak at low energies followed by slowly varying tails above $\sim$30 MeV/nucleon. We attribute the low energy peak to second stage emission and the tails to coalescence. The abrupt change in the coalescence ratios at $\sim$30 MeV/nucleon is consistent with the cut made at this energy per nucleon between the two reaction stages. (See Sec. III C.) The relatively small energy dependence of the tails is due to slow changes in the proton angular distribution with energy, i.e., to the energy dependence of the integral in Eq. (6).

In order to obtain the first stage spectra of composite particles coalescence ratios of the type shown in Fig. 15 were determined for all multiplicity intervals. The tails were fitted with exponential functions of the form $\exp(a+b\text{KE}/n)$ over the range $30 \leqslant \text{KE}/n \leqslant 100$ MeV. These exponentials were then extrapolated down to KE=0, which cut significantly under the peaks of the coalescence ratios. The stage one A^2dN/pdE spectra for the light nuclear fragments were obtained by solving the equation (e.g., for deuterons)

$$\frac{\text{proton}^2}{\text{deuteron}} = \exp(a + b\text{KE}/n) \tag{7}$$

for first stage deuterons, i.e.,

$$\text{deuteron}_1 = \frac{\text{proton}_1^2}{\exp(a + b\text{KE}/n)}, \tag{8}$$

where proton_1 is the first stage proton component and deuteron_1 is the derived first stage deuteron spectrum. Stage one spectra for the other composite particles were obtained the same way. The derived first stage KE/n spectra $AdN/d\text{KE}$ were obtained from the A^2dN/pdE distributions over the range $0 \leqslant \text{KE}/n \leqslant 100$ MeV by multiplying them by p/A. The stage one coalescence distributions were normalized to all the data without any p_x cut by making the sums of the spectra agree for $\text{KE}/n \geqslant 60$ MeV, well outside the range of stage two particles. The slopes of the entire KE spectra and the stage one component derived from coalescence agreed very well for $\text{KE}/n \geqslant 40$ MeV (which is independent of the normalization).

We obtained the second stage components from the experimental spectra for the various particles by subtracting the first stage components. Figure 16 shows typical examples of the KE/n spectra of the composite $Z=1$ and $Z=2$ particles with the decomposition into first and second stages.

E. Results

The results of the above analyses are presented in Fig. 17, which shows the fraction of light particles remaining after first stage removal as a function of multiplicity. While over

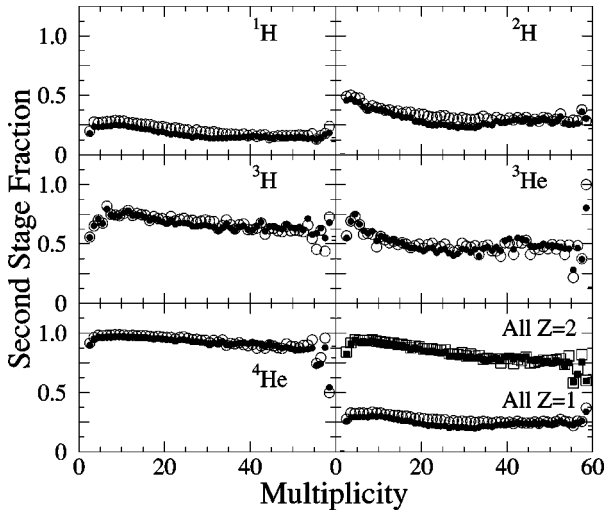

FIG. 17. Fractional particle yields associated with second stage as a function of multiplicity. Solid points, constant velocity cut; open points, deconvolution of spectra.

90% of the α particles as well as $\sim 70\%$ of the tritons are emitted in the second stage, most of the other light particles are associated with the prompt stage. Thus only $\sim 20\%$ of the protons are emitted from the remnant. Recalling from Sec. III A that fragments with $Z \geqslant 3$ are emitted virtually only in the second stage, our results indicate that the equilibrium fraction increases markedly with Z between $Z=1$ and $Z=3$. This increase can be understood from the decrease with increasing mass in the coalescence yield of first stage particles. Figure 17 also shows that the second stage yield is a slowly decreasing function of m for all particles. It is worth noting that both methods used to separate the two stages yield essentially identical results, suggesting that systematic errors in the procedure are small.

Figure 18 shows the average second stage multiplicity m_2 as a function of m. We see that m_2 is a linear function of m and accounts for approximately one-third of the total number of charged particles and fragments. It is evident that the removal of prompt particles is essential in any consideration of equilibrium processes. However, the linearity of the relation between m_2 and m indicates that either multiplicity can be used as a measure of temperature (see Sec. IV C) [17,37].

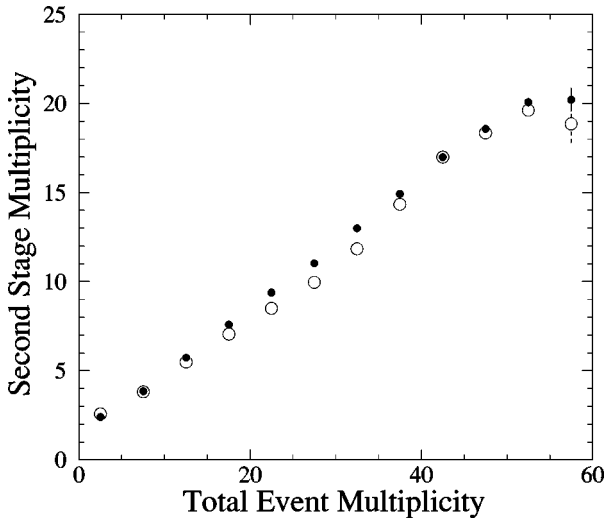

FIG. 18. Variation of second stage multiplicity m_2 with total charged particle multiplicity m. Symbols are defined in Fig. 17.

IV. PROPERTIES OF THE REMNANT

The emission of first stage particles results in the formation of an equilibrated nucleus termed the remnant, which eventually undergoes multifragmentation in the second reaction step. In this section we characterize the remnant by its average charge, mass, excitation energy per nucleon, and temperature. These properties are determined as a function of the event charged particle multiplicity and, along with several other quantities, are tabulated in Table II.

A. Charge and mass

The charge and mass of the projectile remnant can be determined by subtracting the total charge and mass of the preequilibrium particles from $Z=79$ and $A=197$, respectively. In order to obtain the mass, we have estimated the number of first stage neutrons from the corresponding number of protons. We have assumed a value of 1.70 for the prompt n/p ratio, as predicted by the ISABEL cascade simulation [23]. The total number of first stage neutrons includes those which have coalesced into heavier preequilibrium particles.

The average charge and mass of the remnant are plotted as a function of m in Fig. 19. (The mass was incorrectly plotted in Ref. [25].) Both quantities decrease by about a factor of 2 over the event multiplicity range. Figure 20 shows the rms width of the distribution in remnant masses at a given multiplicity expressed as a percentage of the average mass. The rms width increases with m, ranging from approximately 1% to 13%. Comparable fluctuations are seen in the average charge of the remnant. These fluctuations must in large measure reflect the stochastic features of the dynamics.

B. Excitation energy

The excitation energy per nucleon, E^*/A, of the fragmenting projectile remnant is based on an energy balance between the initial stage of the excited remnant and the final stage of noninteracting fragments. The prescription [32] for calculating the excitation energy per nucleon for each event is then

$$\frac{E^*}{A} = \left(\frac{1}{A_{\text{remnant}}}\right)\left[\sum (\text{KE}_i + Q_i) + 3nT/2\right], \qquad (9)$$

where n is the multiplicity of neutrons in the second stage of the reaction, KE_i is the kinetic energy of the ith fragment in the reference frame of the remnant, and Q_i is the removal energy. Since the binding energy per nucleon saturates for even moderately sized nuclei, two approximations were used to calculate the removal energies. First, the initial binding energy per nucleon is assumed to be that of gold since the heavy remnant will have similar binding energy per nucleon. Second, removal energies are negligible for all but the lightest fragments, and were only included for isotopes through carbon. To check these approximations, the removal energies

TABLE II. Dependence of experimental and derived quantities on event charged particle multiplicity.

Multiplicity interval	Multiplicity probability	Second stage multiplicity m_2	Remnant charge $Z_{\rm rem}$	Remnant mass $A_{\rm rem}$	Remnant excitation energy per nucleon, E^*/A (MeV/nucleon)	Remnant temperature T_i (MeV)
1–5	0.146	2.4±0.01	76.0±0.04	194±0.03	1.9±0.02	5.1±0.02
6–10	0.253	3.9±0.01	75.0±0.03	188±0.04	2.4±0.01	5.8±0.01
11–15	0.198	5.7±0.02	72.0±0.04	180±0.07	3.2±0.01	6.6±0.01
16–20	0.137	7.6±0.03	68.3±0.05	172±0.09	4.0±0.02	7.5±0.02
21–25	0.090	9.3±0.04	64.6±0.07	162±0.13	5.0±0.03	8.3±0.03
26–30	0.059	11.0±0.06	61.1±0.09	153±0.17	5.9±0.04	9.1±0.03
31–35	0.044	13.8±0.07	57.5±0.11	144±0.21	7.3±0.05	10.1±0.05
36–40	0.032	14.9±0.09	54.2±0.14	135±0.28	9.0±0.10	11.4±0.08
41–45	0.022	17.0±0.11	51.4±0.16	126±0.33	10.7±0.11	12.7±0.11
46–50	0.013	18.6±0.15	47.7±0.22	116±0.46	12.3±0.13	13.7±0.13
51–55	0.004	20.1±0.26	44.8±0.41	108±0.89	14.0±0.30	14.7±0.22
56–60	0.001	20.2±0.66	38.8±0.93	92±2.10	15.8±0.62	15.6±0.47

Freeze-out temperature $T_{\rm HeDT}$ (MeV)	Remnant density ($\times\rho_0$)	Freeze-out density ($\times\rho_0$)	Remnant entropy per nucleon	Freeze-out entropy per nucleon	Radial flow energy (MeV/nucleon)
3.6±1.03	0.99±0.0002	0.77±0.336	0.74±0.002	1.09±0.003	0.0±0.14
3.8±0.08	0.95±0.0003	0.63±0.021	0.84±0.001	1.09±0.002	0.1±0.01
4.0±0.02	0.92±0.0005	0.52±0.005	0.97±0.001	1.13±0.002	0.2±0.02
4.2±0.05	0.87±0.0007	0.43±0.008	1.10±0.002	1.20±0.003	0.4±0.01
4.7±0.11	0.82±0.0010	0.40±0.014	1.24±0.003	1.27±0.004	0.6±0.06
5.1±0.12	0.77±0.0013	0.36±0.013	1.38±0.004	1.34±0.005	1.0±0.07
5.5±0.11	0.73±0.0018	0.32±0.010	1.54±0.005	1.43±0.006	1.5±0.09
5.9±0.14	0.68±0.0026	0.27±0.010	1.72±0.007	1.51±0.008	2.5±0.11
6.2±0.11	0.64±0.0032	0.24±0.008	1.92±0.010	1.61±0.012	3.4±0.14
6.3±0.15	0.59±0.0040	0.19±0.008	2.09±0.011	1.76±0.017	5.1±0.19
6.6±0.28	0.54±0.0069	0.17±0.012	2.25±0.019	1.92±0.035	5.8±0.26
5.7±0.73	0.48±0.0117	0.11±0.022	2.49±0.034	2.38±0.097	7.7±0.56

for several events were summed using the removal energies from the actual remnant. The values obtained were typically 1%–2% higher than the approximate value.

We must make an estimate of the average kinetic energy of second step neutrons and so have assumed a Maxwell-Boltzmann thermal distribution, consistent with volume emission [38]. In Eq. (9) we substitute

$$T=\sqrt{E^*/a}, \tag{10}$$

where a represents the level density parameter of the degenerate Fermi gas. A value of $a=A/13$ is assumed in agreement with empirical studies [39]. A quadratic equation in $\sqrt{E^*/A}$ is obtained and solved for E^*/A. Only one physical solution exists. The number of second stage neutrons, n, was obtained as the difference between the mass of the remnant and the sum of the masses of the second stage particles and fragments. We estimate that n increases from $\sim$15 for low m to $\sim$20 for intermediate m and then decreases to $\sim$10 for the highest m.

The above prescription for the calculation of the remnant excitation energy was tested on simulated events from a first stage cascade model (ISABEL) [23] plus a statistical multifragmentation model (SMM) [19]. Twenty thousand iterations for 1A GeV Au+C were performed. The simulation ISABEL reports an excitation energy and remnant mass and charge while the SMM distributes this energy to fragments as kinetic energy and removal energy. Good agreement with the ISABEL E^*/A values was found when the SMM results were analyzed by means of Eq. (9).

The resulting values of the mean excitation energy per nucleon at a given m, $\langle E^*/A\rangle$, are shown in Fig. 19. Excellent agreement is obtained between the values based on the two methods of preequilibrium removal, indicating that systematic errors due to this source are small. A possible systematic error in the source velocity, $\sim$1% at most, changes the $\langle E^*/A\rangle$ by a comparable amount. A $\pm$5% shift along the rigidity axis in the individual isotopic bands in Fig. 2 introduces a systematic shift that is smaller than the statistical uncertainty. The corrections for TPC efficiency discussed in Sec. II C increase the $\langle E^*/A\rangle$ values by $\sim$3%.

The largest systematic error is associated with the estimate of the mean energy of the second stage neutrons. We have estimated the magnitude of this error by assuming a mean neutron energy of $2T$, corresponding to surface emission [38]. We have also examined the effect of changing the level density parameter over a reasonable range, from A/13

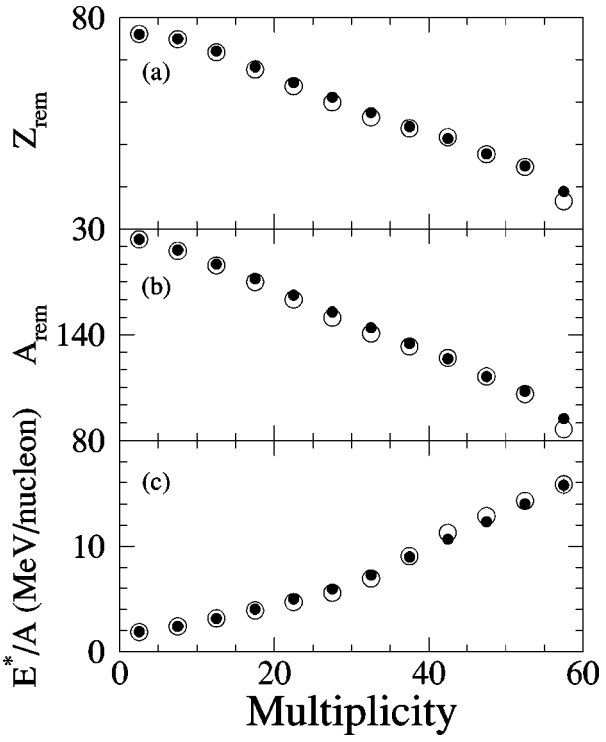

FIG. 19. Properties of the remnant as a function of m: (a) remnant charge, (b) mass, and (c) excitation energy per nucleon, E^*/A. Symbols are defined in Fig. 17.

to $A/10$. A larger value of a will yield a lower temperature and, as a result, less energetic neutrons. Finally, we have used a temperature representing an average over the expansion and cooling of the remnant. This temperature was obtained as the mean of the remnant temperature, given in Sec. IV C, and the freeze-out temperature, discussed in Sec. V A. On the basis of these calculations we estimate a systematic error of $\pm 10\%$ in $\langle E^*/A \rangle$ due to our assumptions about second stage neutron emission. The uncertainty in the number of neutrons is small compared to the uncertainty in their average energy. We have focused on systematic errors in the excitation energy of the remnant because the other properties of the remnant are less affected by errors of this type.

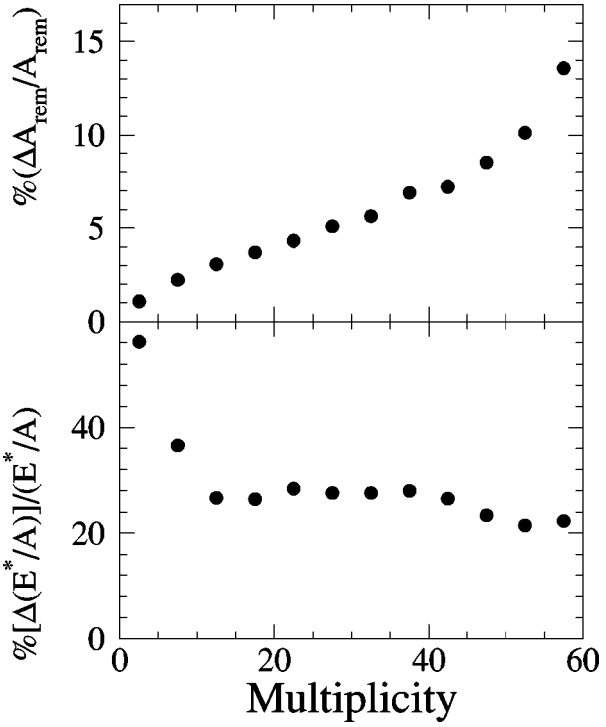

FIG. 20. rms width of the distribution in A_{rem} (top) and E^*/A (bottom) at the given multiplicities expressed as percent.

The fluctuations in $\langle E^*/A \rangle$ are shown in Fig. 20. The rms width of the $\langle E^*/A \rangle$ distribution at a given m is approximately 27%, independent of m for $m > 10$. This width reflects the combined effect of the fluctuations in E^* and in those of A_{rem}, discussed above. In addition to dynamical effects, the assumptions about the number and energy of the first stage neutrons presumably also contribute to the width.

Figure 19 shows that $\langle E^*/A \rangle$ varies approximately as m^2. This trend is the combined result of the variation of E^*, which is approximately linear in m, and that of A, which varies inversely with m. The actual E^* ranges up to ~ 1500 MeV and has an average value of ~ 850 MeV over the multiplicity range for which MF occurs to a significant extent, $m \sim 10$–60.

The value of E^* per nucleon knocked out of the gold nucleus, designated α, decreases with increasing multiplicity from ~ 35 MeV/nucleon to ~ 25 MeV/nucleon. The cascade code ISABEL yields a value of $\alpha \sim 30$ MeV/nucleon [23]. Boltzmann-Uehling-Uhlenbeck (BUU) calculations reported for Au on Cu [40] indicate that α is ~ 12 MeV/nucleon for central and midcentral collisions and increases to over 40 MeV/nucleon for the most peripheral collisions. Since these collisions correspond to low m, the qualitative trend is similar to the present trend. A recent estimate based on the statistical abrasion model [41] gives $\alpha \sim 27$ MeV, again in qualitative agreement with the above values.

C. Temperature

The temperature of the remnant was obtained from $\langle E^*/A \rangle$ according to the ideal Fermi gas model. We have assumed that the prompt knockout step does not affect the volume of the gold nucleus but instead reduces its density. The chemical potential μ and initial temperature T_i, averaged for neutrons and protons, were determined implicitly from the density $\rho = A/V_{Au}$ and $\langle E^*/A \rangle$ by

$$\rho = \left(\frac{g}{\lambda^3} \right) f_{3/2}(z), \tag{11}$$

where $g = 4$ is the product of the spin and isospin weight factors for nucleons, $\lambda = h/(2\pi m T)^{1/2}$ is the nucleon thermal wavelength, $z = \exp(\mu/T)$ is the fugacity,

$$f_n(z) = \frac{1}{\Gamma(n)} \int_0^\infty \frac{x^{n-1}}{z^{-1} e^x + 1} dx, \tag{12}$$

and

$$\frac{E^*}{A} = \frac{3}{2} T \frac{f_{5/2}}{f_{3/2}} - \frac{3}{5} \epsilon_F, \tag{13}$$

with Fermi energy $\epsilon_F = (h^2/8m\pi^2)(6\pi^2\rho/g)^{2/3}$.

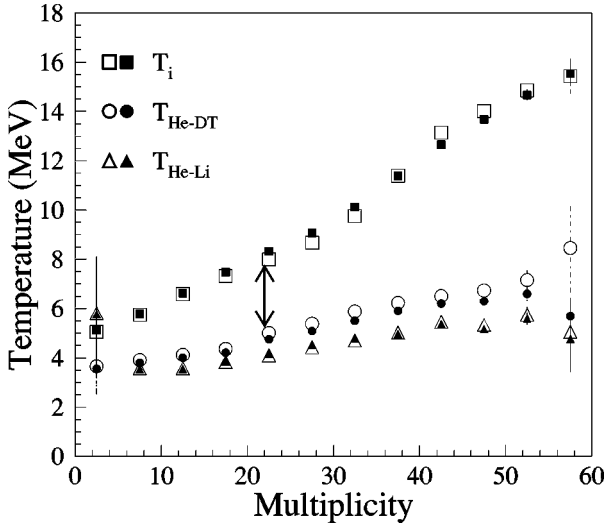

FIG. 21. Variation of initial and freeze-out temperatures with multiplicity. Symbols are defined in Fig. 17. The double-headed arrow marks the critical multiplicity [42].

Figure 21 shows that T_i is an approximately linear function of multiplicity over the range for which MF occurs. We have previously determined the critical multiplicity, i.e., the multiplicity at the critical point, by means of power law fits to the second moment of the fragment charge distribution and reported the value $m_c=26\pm1$ [17]. More recently, we have redetermined m_c by a different procedure in which the fragment charge distribution was fit directly [42]. It was found that $m_c=22\pm1$. At this multiplicity $T_i=8.3\pm0.6$ MeV, where most of the uncertainty is due to the systematic errors. The fluctuations in $\langle E^*/A\rangle$ at m_c lead to a spread of ±1.1 MeV in the value of T_i at this multiplicity.

V. FROM REMNANT TO FRAGMENTS

In this section we examine some aspects of the remnant's evolution to the final multifragment state. We focus on the freeze-out temperature, the caloric curve, the expansion as viewed in the temperature-density plane, the change in entropy, and the radial flow generated in the expansion. We begin by presenting some of our results on fragment yields.

A. Fragment yields

As mentioned in the Introduction, the evolution of the fragment yield distribution with excitation energy or multiplicity can help define the regime where MF is of importance. Figure 22 shows the fragment charge yield distribution for several multiplicity intervals. Similar results have been reported by Kreutz *et al.* [40]. At low multiplicities the yields of light particles and fragments drop off steeply with increasing Z. The yield of intermediate-mass fragments (IMF's) with $Z=3$–30 is suppressed by several orders of magnitude relative to that of the lightest particles. This is the regime where light particles are emitted in the first stage as well as by evaporation. The emission of these light particles leads to the formation of heavy spallation products, whose yield peaks at $Z\sim70$. The peak at $Z\sim40$ is due to fission. This process is of importance at the modest excitation energies, $E^*/A\leqslant2$ MeV/nucleon, which correspond to these multiplicities. Multifragmentation is not important in this regime.

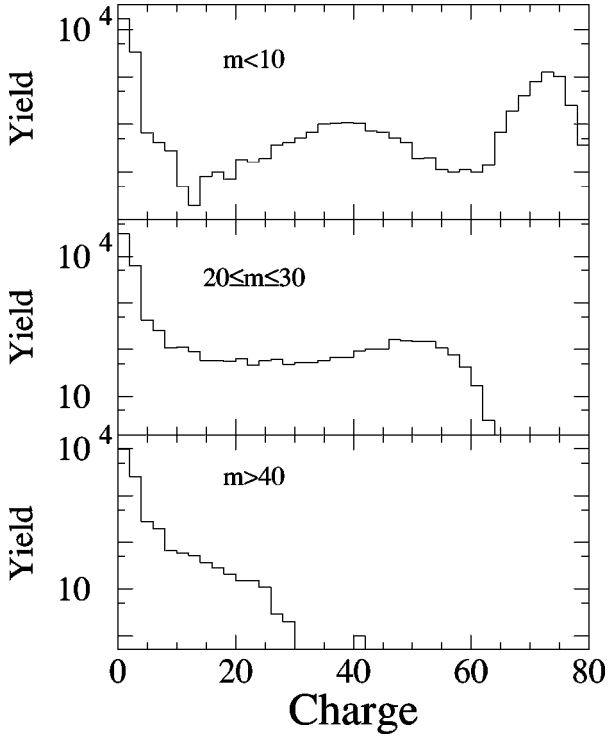

FIG. 22. Charge yield distribution at the given multiplicities.

At intermediate multiplicities there is a broad distribution of yields. This is the regime where the yields of IMF's obey a power law and where the continuous phase transition formalism has been applied [17,18]. In this picture, the rather flat portion of the yield distribution above $Z\sim20$ is due to finite size effects. In a small system the bulk liquid gives way to a single largest fragment, the yield of which accounts for the distribution at large Z.

At the highest multiplicities, the yields of light particles and fragments once again decrease sharply with increasing Z. This is the regime where breakup of the nucleus into individual nucleons and light particles, a process akin to vaporization, becomes important.

The multiplicity distribution of IMF's has been studied by the ALADIN Collaboration [14,15] who described their results as ''the rise and fall of multifragment emission.'' Figure 23 shows the multiplicity distribution of IMF's obtained in the present work. As already noted, IMF production becomes significant at $m\geqslant10$ and reaches its maximum of ~4.5 IMF per interaction at $m=42$–52, in agreement with the ALADIN results [15]. Note that the number of IMF's at the critical multiplicity is only ~1.2, on average.

The present distribution is essentially a mirror image of the ALADIN distribution because m is inversely related to $Z_{\rm bound}$, the abscissa variable used in that work. The poor statistics of events with $m>60$ prevents us from extending the decreasing part of the IMF distribution any further. The ALADIN data [15] show that for a target as light as carbon, the maximum excitation energy deposited in the projectile remnant is too low to reach the region of complete vaporization.

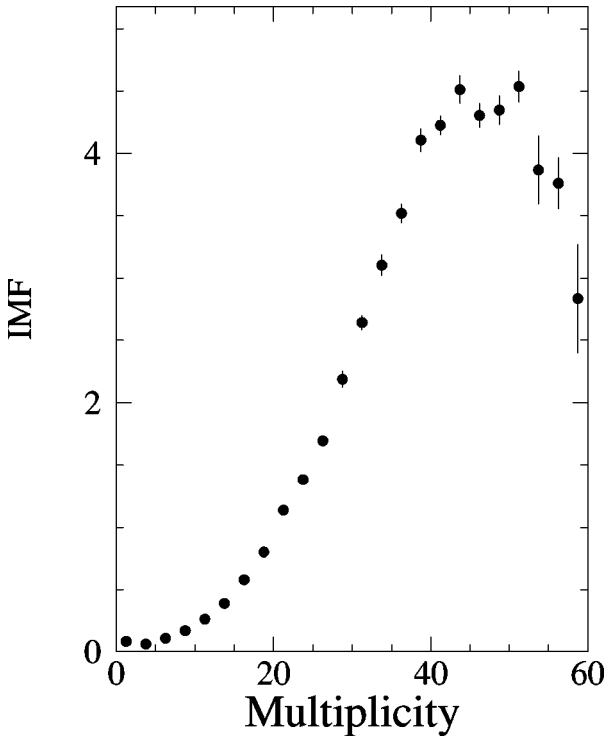

FIG. 23. IMF ($Z=3$–30) multiplicity distribution as a function of event charged particle multiplicity.

B. Freeze-out temperature

Considerable evidence has been obtained indicating that the remnant expands and cools prior to breakup, with freeze-out occurring at a temperature T_f [8–10,43]. If we assume that thermal and chemical equilibrium is reached after the spectator remnant expands and cools, then the freeze-out temperature can be computed using the double ratio of isotope yields of the form [44]

$$\frac{Y(A,Z)/Y(A+1,Z)}{Y(A',Z-1)/Y(A'+1,Z-1)}. \tag{14}$$

These ratios have been used in a recent study [24] to calculate nuclear temperatures based on helium and lithium isotopes. On the assumption that these nuclides are formed only in their ground states, the temperature is given by

$$T_{\mathrm{HeLi}}=\frac{13.3\ \mathrm{MeV}}{\ln\left[2.19\times\dfrac{Y(6,3)/Y(7,3)}{Y(3,2)/Y(4,2)}\right]}. \tag{15}$$

The T_{HeLi} obtained in this fashion are plotted as a function of m in Fig. 21. Various systematic errors affect these temperatures. The ^{3}He/^{4}He ratio is affected by the preequilibrium removal cut for ^{3}He, which is much more important than that for ^{4}He. A 5 MeV/nucleon shift in the location of this cut affects this ratio by $\sim$20%. Both ^{3}He/^{4}He and ^{6}Li/^{7}Li ratios are affected by systematic shifts in the boundaries of the dE/dx vs rigidity plots, Fig. 2, such that the yield of one isotope increases while that of the neighboring isotope decreases. The worst case scenario would involve an increase (decrease) in the ^{6}Li yield with respect to the ^{7}Li yield and a simultaneous decrease (increase) in the ^{3}He yield relative to that of ^{4}He. For example, a 10% shift in the two particle identification bands leading to an increased yield of both ^{6}Li and ^{4}He would result in a 50% increase in the ratio of the yields in Eq. (15).

It can be shown that the fractional error in the temperature due to systematic errors in yields is approximately

$$\frac{\Delta T_{\mathrm{HeLi}}}{T_{\mathrm{HeLi}}}\sim 0.075\times T_{\mathrm{HeLi}}\frac{\Delta Y_R}{Y_R}, \tag{16}$$

where

$$Y_R=\frac{Y(6,3)/Y(7,3)}{Y(3,2)/Y(4,2)}.$$

This result shows that the fractional error in T_f increases with T_f. The combined effect of the two illustrations given above would lead to a 20% error in a temperature of 5 MeV.

As noted above, the values of T_{HeLi} plotted in Fig. 21 have been obtained on the assumption that the population of excited states is negligible. ^{6}Li has known excited states at 2.185 MeV and 3.562 MeV while ^{7}Li has an excited state at 0.478 MeV [45]. These states decay at least partially to the corresponding ground states by γ-ray emission. The inclusion of these states in Eq. (15) has been examined by Campi *et al.* [46]. They find that, for E^*/A corresponding to the critical multiplicity, T_{HeLi} is $\sim$10% lower when the excited states of the Li isotopes are included.

We have also used a T_{HeDT} thermometer, based on the ratio of deuteron and triton yields as well as on that of the He isotopes. These nuclides do not have any low-lying excited states and consequently the following expression, analogous to Eq. (15), can be used without correction for γ decay from excited states [44]:

$$T_{\mathrm{HeDT}}=\frac{14.3\ \mathrm{MeV}}{\ln\left[1.60\times\dfrac{Y(4,2)/Y(3,2)}{Y(3,1)/Y(2,1)}\right]}. \tag{17}$$

In addition, the uncertainty in the separation between the d and t bands in Fig. 2 is much smaller than that between the ^{6}Li and ^{7}Li bands and the statistical error is also reduced substantially. To be sure, the first stage cut is larger for this thermometer but, as noted above, the effect of this correction on the temperature is relatively small. We therefore believe that the T_{HeDT} are more robust than the T_{HeLi}.

Figure 21 shows the results for T_{HeDT}. While these temperatures are uniformly higher than the corresponding T_{HeLi} the differences are small. Both sets of freeze-out temperatures are a linear function of m, although the variation with m is much smaller than that of the remnant temperature. The values of T_f are always lower than the corresponding values of T_i, the difference increasing from 1 or 2 MeV for small m to $\sim$8 MeV for large m. The value of T_f at the critical multiplicity is $T_f=4.7\pm0.4$ MeV. The critical temperature of the nucleus must lie somewhere between the initial and freeze-out temperatures at this multiplicity, i.e., between 4.7 $\pm$0.4 MeV and 8.3$\pm$0.6 MeV. The linearity with m of both T_i and T_f suggests that the temperature at which the fragments are first formed, which is bracketed by these two temperatures, is also a linear function of m. This linearity indi-

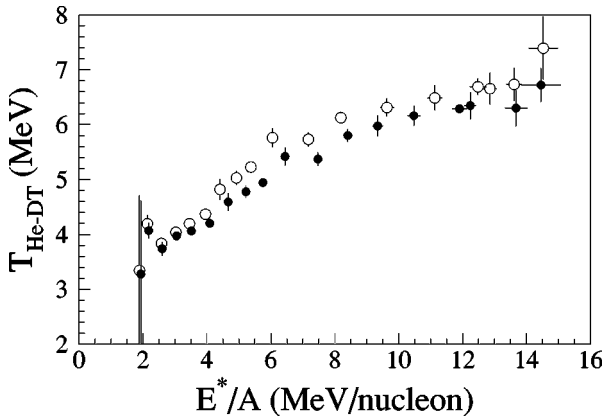

FIG. 24. ''Caloric curve'' for 1A GeV Au+C: plot of T_{HeDT} vs E^*/A. Symbols are defined in Fig. 17.

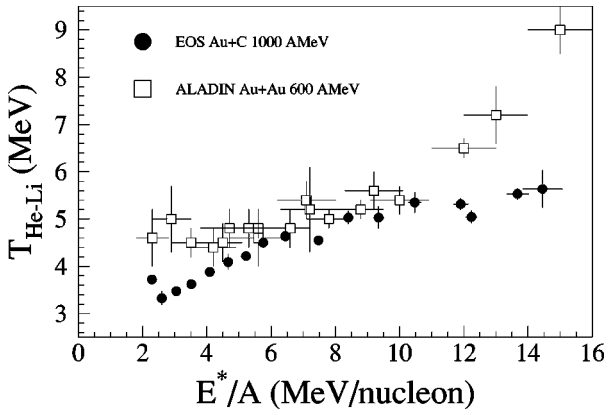

FIG. 25. Comparison of T_{HeLi} vs E^*/A with the ALADIN curve [24]. The temperature has been multiplied by 1.2 to make it comparable to the ALADIN data.

cates that multiplicity is a valid measure of temperature, confirming one of the assumptions in the determination of the critical exponents [17].

The validity of freeze-out temperatures obtained by the method of double isotope yield ratios has become a subject of recent scrutiny. Various groups have investigated the effects of side feeding, radial flow, final state interactions, and quantum statistics [47–52]. It appears that these factors have a relatively small ($\sim$10%) effect on the temperatures provided that their values do not exceed $\sim$7 MeV.

C. Correlation between T_f and $\langle E^*/A\rangle$

Pochodzalla *et al.* [24] have recently presented a plot of T_{HeLi} versus $\langle E^*/A\rangle$ of the remnant for 600A MeV Au+Au and interpreted this curve as a ''caloric'' curve. Their curve is indeed similar to the caloric curve of water and has been interpreted by the authors as evidence for a first-order phase transition. Although the interpretation of this correlation has been questioned on various grounds [46,53,54], it is nonetheless worthwhile to examine the present results from this point of view. Figure 24 shows our values of T_{HeDT} as a function of $\langle E^*/A\rangle$. The temperature shows a smooth, monotonic increase with excitation energy per nucleon. De *et al.* [55] have recently obtained a caloric curve for finite nuclei on the basis of a Thomas-Fermi model. The shape of their curve for ^{150}Sm closely resembles that in Fig. 24, although their temperatures are somewhat higher than ours for the same E^*/A.

Our results are compared with the ALADIN curve [24] in Fig. 25. To make the comparison as close as possible, we show our less robust values of T_{HeLi}. They have been multiplied by 1.2 to duplicate the procedure followed in Ref. [24] to correct for side feeding. Although the two data sets are consistent over much of the energy range, there is a definite difference in shape. The ALADIN curve is essentially flat between 2 and 10 MeV/nucleon and increases sharply at higher excitation energies. In contrast, our curve shows a monotonic increase that becomes less pronounced at the highest $\langle E^*/A\rangle$. We believe that the separation of the first and second stage particles is more straightforward for the Au+C reaction than for the Au+Au reaction. Furthermore, the experimental determination of the number and energy of the second stage $Z=1$ particles in the present work makes the determination of the $\langle E^*/A\rangle$ values more accurate than the estimate made by Pochodzalla *et al.* [24], although this advantage is mitigated to some extent by their neutron data. Finally, it should be noted that the difference in dynamics in the two reactions may introduce a significant difference at higher values of $\langle E^*/A\rangle$. Thus, the mass of the remnant at high $\langle E^*/A\rangle$ is nearly twice as large in the present work as in Ref. [24].

D. Trajectories in the T-ρ plane

The evolution of highly excited nuclear systems in the temperature-density (T-ρ) plane is of long-standing interest in connection with the equation of state of nuclear matter [4,56,57]. On the assumption that the remnant expands isentropically to the MF freeze-out state, an assumption that is justified in the next section, trajectories in the T-ρ plane can be constructed in the following manner.

In an isentropic expansion the final volume V_f is related to the initial volume V_i by

$$V_f = V_i\left[\frac{T_i}{T_f}\right]^{3/2}. \tag{18}$$

This relation is valid for a nondissipative Fermi gas. The initial volume is assumed to be the unexpanded gold volume. The initial and final densities ρ_i and ρ_f can be obtained using the previously determined remnant masses. The results are displayed in Fig. 26. Both ρ_i and ρ_f decrease with increasing m. The decrease in ρ_i reflects the increasing number of holes in the Fermi sea of the remnant while that in ρ_f is due, in addition, to the expansion. At the critical multiplicity ($m_c = 22\pm 1$) the freeze-out density is approximately one-third that of normal nuclear matter.

Isentropic trajectories for the expanding remnant based on Eq. (18) are sketched in Fig. 27. The initial hot remnant is driven toward lower ρ and T by the expansion. The trajectories for multiplicities previously identified as the critical region [17] are shown as bold lines. These trajectories reach the vicinity of $\rho_c \sim (0.3–0.4)\rho_0$ and $T_c \sim 5–8$ MeV, in reasonable agreement with theoretical predictions for the critical region of finite, charged nuclei [56,58]. Assuming the initial volume is not the gold volume but a normal nuclear density

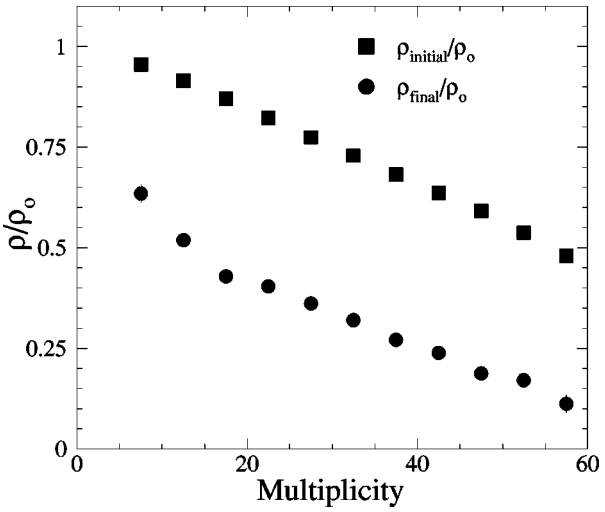

FIG. 26. Initial and final densities as a fraction of normal nuclear density versus m.

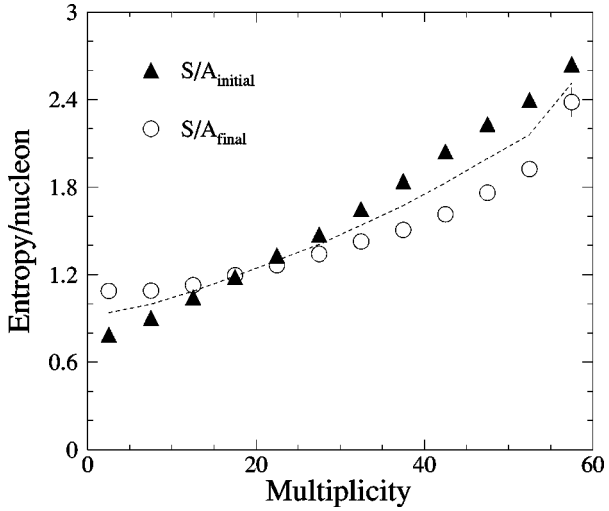

FIG. 28. Initial and final entropy/nucleon versus m. The dashed curve corresponds to the average entropy/nucleon.

volume associated with the remnant mass changes the range of the ρ_f/ρ_0 ratios from 0.1–0.6 to 0.2–0.6. This assumption would cause the trajectories of the highest-multiplicity bins to enter the region identified by theoretical studies at lower temperatures.

Trajectories in the T-ρ plane have previously been obtained on the basis of various theoretical models [59–61]. These models differ in their predictions of the regions of the phase diagram populated by the calculated trajectories. The present results may provide a useful constraint on these models.

E. Entropy change

In this section we examine the assumption of an isentropic expansion made in Sec. V D and show that it is consistent with the results given there. We have used the statistical formulation of Bondorf *et al.* [62] to compute event by event the final entropy per nucleon. In this model the entropy of each fragment in the final state is obtained as the sum of bulk, translational, and surface terms. The translational contribution is calculated by considering all fragments as making up an ideal gas confined to a free volume. To obtain the free volume we subtract the volume of the remnant at normal density from the final expanded volume, V_f, computed in Sec. V D. This calculation then accounts for the fact that the fragments occupy a volume which includes that space produced through both the expansion and from the knockout of the prompt nucleons.

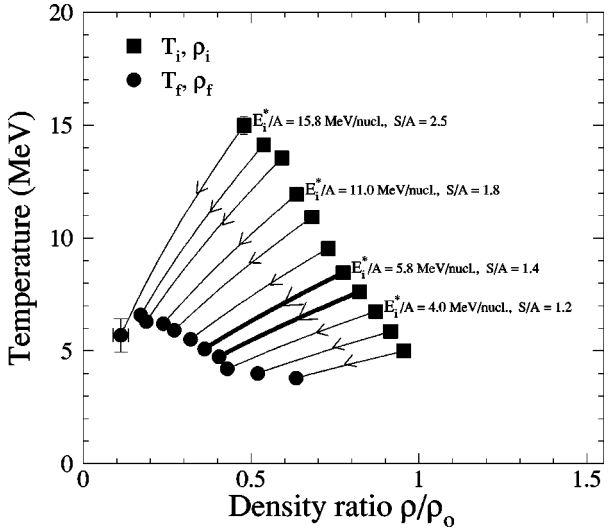

FIG. 27. Trajectories in the T-ρ plane for different multiplicities. The points corresponding to the remnant (squares) are labeled with its excitation energy and entropy per nucleon. Trajectories in the vicinity of the critical region are in boldface.

The above approach cannot be followed in the evaluation of the initial entropy of the remnant because of the lack of an independent determination of the remnant temperature. Instead, the remnant temperature was obtained in Sec. IV C from the excitation energy by means of the Fermi gas model. To be consistent, we use this same model to evaluate the entropy of the remnant.

The results of this analysis are displayed in Fig. 28. Both the initial and final entropy per nucleon increase with multiplicity from $\sim$1 to 2.5 and agree with each other to within $\sim$12%, on average. It should be noted that this agreement does not prove that the expansion is isentropic. Our analysis is somewhat circular in that we obtained V_f on the assumption of constant entropy and then used this volume to evaluate the translational entropy of the final state. The dependence of the translational entropy on V_f is rather weak, however (i.e., it is logarithmic), and the other entropy terms are independent of V_f. Thus, the final volume does not impose a major constraint on the entropy. We conclude that the results are consistent with an isentropic expansion.

F. Collective radial flow

In recent years it has become evident that fragment kinetic energies have a contribution from radial flow. This effect, which may arise from thermal pressure or from compression, is particularly significant at energies of $\sim$100 MeV/nucleon and above in central collisions of nearly symmetric nuclei [63–67]. For example, the average fractional contribution of radial flow to the kinetic energies of deuter-

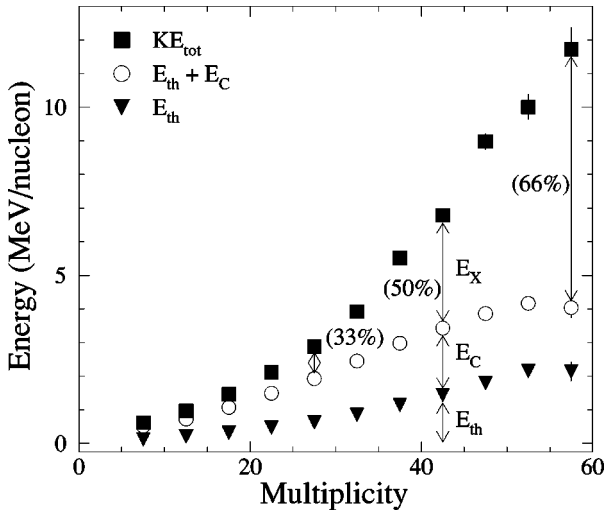

FIG. 29. Energy per remnant nucleon versus multiplicity. Squares represent the total kinetic energy of all charged second stage particles. Percentages refer to E_X as a fraction of $\mathrm{KE_{tot}}$.

ons and α particles emitted in central collisions of (0.25–1.15)A GeV Au plus Au is 45% and 60%, respectively [67]. We examine here whether similar effects may be present in the highly asymmetric interaction of present interest.

We focus on the mean transverse kinetic energy $\langle \mathrm{KE}_t \rangle$ of fragments with $Z \geqslant 3$, i.e., fragments formed only in the second stage. The values of $\langle \mathrm{KE}_t \rangle$ were obtained by averaging over the KE_t distributions. The KE_t values were, in turn, obtained from the corresponding p_t. In order to reduce the statistical error we did not separate the individual isotopes corresponding to a particular nuclear charge.

The values of $\langle \mathrm{KE}_t \rangle$ for all second stage charged particles were summed and converted to total kinetic energy ΣKE, where $\Sigma \mathrm{KE} = 3/2 \Sigma \langle \mathrm{KE}_t \rangle$. This procedure yields a more accurate value of ΣKE than the summation of the actual kinetic energies because the latter are subject to the error arising from the transformation between the laboratory and remnant frames. The resulting values of ΣKE/nucleon are plotted versus multiplicity in Fig. 29. The variation with m parallels that of E^*/A (Fig. 19), which is not surprising since the kinetic energy of charged particles is the chief component of the excitation energy.

In order to determine whether radial flow is present we assume that the initial remnant undergoes expansion to freeze-out with no decrease in nucleon number. This assumption is justified by the short time required for the expansion (discussed below). Conservation of energy then allows us to decompose ΣKE into three sources:

$$\sum \mathrm{KE} = E_{\mathrm{th}} + E_C + E_X , \tag{19}$$

where E_{th} is the sum of the translational thermal contributions to the fragment spectra, E_C is the Coulomb contribution, and E_X is what remains when the other terms are subtracted from ΣKE. Within the spirit of the calculation of the final state temperature, each final state charged particle originating in the breakup of the remnant will contribute $\frac{3}{2} T_f$ to E_{th}. The total Coulomb energy available for doing work is given by the difference in the self-energy of the remnant and the sum of the self-energies of all the second stage particles. Thus,

$$E_C = \frac{3}{5} e^2 \left(\frac{Z_R^2}{R_{\mathrm{Au}}} - \sum \frac{Z_f^2}{R_f} \right). \tag{20}$$

With Eq. (19), E_X can be calculated for the experimental data. This quantity, displayed in Fig. 29 as a function of m, increases from 0 to nearly 8 MeV/nucleon with increasing m, thus accounting for a substantial fraction of ΣKE, $\sim$30% at midmultiplicities and up to $\sim$66% at the largest m. As a test of the validity of Eq. (19) in accounting for the total kinetic energy we have applied it to spectra generated by the two-step model described in Sec. IV B, which used the cascade code ISABEL [23] followed by the statistical multifragmentation model SMM [19], where flow was not included in the SMM. The freeze-out temperature, which is needed to determine E_{th}, was obtained using the Albergo procedure [44] and was found to be in good agreement with the experimental T_f. This procedure yields E_X consistent with zero, as expected. It also shows that a statistical model without flow cannot fit the experimental transverse energies [68].

The missing term in Eq. (19) is the collective expansion energy and we therefore attribute E_X to radial flow. The contribution of this flow energy to the total excitation energy of the remnant increases with m and accounts for $\sim$50% of E^*/A at the largest m. However, if the double isotope ratio method were to underestimate T_f for large E^*/A, as suggested by Xi *et al.* [49], then our flow energies at large multiplicities would be correspondingly overestimated.

At the highest multiplicities, which correspond to central collisions, the radial flow velocity β_{radial}, obtained from the above analysis is $\sim$0.13, where $\beta_{\mathrm{radial}} = (2E_X/938)^{1/2}$. This value may be compared with a value of $\sim$0.32 obtained in central 1A GeV Au+Au collisions [67]. The latter is based on results for $Z=1$ and 2 particles and it appears that β_{radial} decreases slowly with the fragment charge, at least for 100A MeV Au+Au collisions [66]. Nonetheless, the present value of β_{radial} for central Au+C collisions is at least a factor of 2 smaller than that for comparable Au+Au collisions. The difference may be attributable to the effect of the compression-decompression cycle in Au+Au, which presumably is not present in Au+C, and also to the larger thermal energy in central Au+Au collisions.

The average time required for the remnant to expand to freeze-out can be estimated. We simply divide the increase in radius, which can be obtained from Eq. (18), by the mean flow velocity $\beta_{\mathrm{radial}}/2$. This estimate yields a short expansion time of about 70 fm/c, in good agreement with expansion times obtained from fragment-fragment correlation studies [69,70] and theoretical predictions [43]. The time is not strongly dependent on multiplicity. Thus, multifragmentation is a very fast process, which suggests a simultaneous disassembly of the remnant. The presence of a significant component of directed sideward flow could affect this time estimate. However, it is unlikely that such flow is of importance in the very asymmetric Au+C collisions. Thus, it is known that directed flow is maximal at intermediate multiplicities [67] whereas the observed value of the flow energy becomes largest for the highest m.

Since the excitation energy of the remnant is fixed by the energy balance, the presence of a radial flow energy must reduce the thermal energy. This reduction has an effect on some of the quantities determined in the preceding sections. The magnitude of this effect depends on the time at which the flow is established. The largest adjustments must be made if the flow is fully developed by the time the equilibrated remnant is formed. Under these conditions, the thermal excitation energy would account for $\sim 85\%$ of E^*/A at midmultiplicities and for only $\sim 50\%$ at the largest m. The caloric curve would become much steeper than shown in Figs. 24 and 25. At the critical multiplicity, the temperature of the remnant would be reduced from 8.3 to 7.8 MeV while the density at freeze-out would increase by some 10%. In addition, the reduction in T_i would reduce the initial entropy and improve somewhat the overall agreement between the initial and final entropy of the system.

VI. SUMMARY

We have presented the results of a reverse kinematics study of the multifragmentation of 1A GeV gold nuclei interacting with carbon. Since the detector system provided nearly complete event reconstruction, we have been able to determine for each event the momentum and charge of the charged particles and fragments resulting from projectile breakup. The masses of fragments with $Z \leqslant 4$ have also been determined for each event while those of heavier fragments were determined on average.

A contour plot of proton p_t versus y as well as the rapidity distributions and spectra of $Z=1$ and $Z=2$ particles show the presence of two distinct components, ascribable to two different reaction stages. The first stage can be described as an intranuclear cascade and involves the emission of energetic (in the moving frame) prompt particles. The second stage involves emission from an equilibrated system. Fragments with $Z>2$ appear to be emitted only in the second stage.

We have developed two distinct methods to separate the particles associated with the two reaction stages and have obtained excellent agreement between them. The importance of the first stage decreases with increasing particle mass; this stage accounts for 80% of the proton yield but only 10% of the α-particle yield. The second stage fractional yields of all $Z=1$ and 2 particles decrease weakly with increasing event charged particle multiplicity m. The second stage charged particle multiplicity is a linear function of m and accounts for $\sim 1/3$ of all charged particles.

The emission of prompt particles leads to the formation of an excited remnant. We have determined the nuclear charge and the average mass, excitation energy per nucleon, and temperature of the remnant as well as the fluctuations in these quantities, as a function of m. The mass decreases from ~ 194 to ~ 92 as m increases from 1 to 60. The excitation energy per nucleon increases nearly quadratically from ~ 2 MeV/nucleon to ~ 16 MeV/nucleon with increasing m. The temperature is an approximately linear function of m and has a value of 8.3 ± 0.6 MeV at the critical multiplicity $m_c = 22 \pm 1$.

The expansion of the remnant to the multifragment freeze-out point has been examined. The freeze-out temperature was determined from two different double isotope ratios and was found to increase linearly with m. The freeze-out temperature corresponding to the critical multiplicity is 4.7 ± 0.4 MeV. The two temperatures obtained at m_c bracket the critical temperature of the nucleus. A plot of the freeze-out temperature versus the excitation energy per nucleon of the remnant shows a smooth, monotonic increase.

The densities of the remnant and of the freeze-out configuration have been determined as a function of m on the assumption of an isentropic expansion. The results permit us to construct trajectories in the temperature-density plane. Trajectories corresponding to the critical region terminate at temperatures and densities that are in agreement with theoretical estimates for the critical region of finite, charged nuclei.

Using a model-independent analysis based on energy conservation we have determined that radial flow is present. The collective expansion energy accounts for an increasing fraction of the kinetic energy of light fragments with increasing m, amounting to $\sim 30\%$ at midmultiplicities. An estimate based on the mean flow velocity indicates that the expansion is fast, occurring in ~ 70 fm/c. The effect of radial flow on the temperature and density of the system has been examined.

This work was supported in part by the U.S. Department of Energy under Contracts or Grants Nos. DE-AC03-76SF00098, DE-FG02-89ER40531, DE-FG02-88ER40408, DE-FG02-40412, and DE-FG05-88ER40437, and by the U.S. National Science Foundation under Grant No. PHY-91-23301.

[1] C. F. Powell and G. P. S. Occhialini, Nature (London) **159**, 93 (1947).
[2] See L. G. Moretto and G. J. Wozniak, Annu. Rev. Nucl. Part. Sci. **43**, 379 (1993) for a recent review.
[3] J. E. Finn *et al.*, Phys. Rev. Lett. **49**, 1321 (1982).
[4] P. J. Siemens, Nature (London) **305**, 410 (1983).
[5] T. J. Schlagel and V. R. Pandharipande, Phys. Rev. C **36**, 162 (1987).
[6] H. Müller and B. D. Serot, Phys. Rev. C **52**, 2072 (1995).
[7] K. C. Chase and Z. Mekjian, Phys. Rev. Lett. **75**, 4732 (1995).
[8] A. M. Poskanzer *et al.*, Phys. Rev. C **3**, 882 (1971).
[9] G. D. Westfall *et al.*, Phys. Rev. C **17**, 1368 (1978).
[10] A. S. Hirsch *et al.*, Phys. Rev. C **29**, 508 (1984).
[11] R. W. Minich *et al.*, Phys. Lett. **118B**, 458 (1982).
[12] M. Mahi *et al.*, Phys. Rev. Lett. **60**, 1936 (1988).
[13] N. T. Porile *et al.*, Phys. Rev. C **39**, 1914 (1989).
[14] J. Hubele *et al.*, Z. Phys. A **340**, 263 (1991); Phys. Rev. C **46**, R1577 (1992).
[15] A. Schüttauf *et al.*, Nucl. Phys. **A607**, 457 (1996).
[16] L. Beaulieu *et al.*, Phys. Rev. C **54**, R973 (1996).
[17] M. L. Gilkes *et al.*, Phys. Rev. Lett. **73**, 1590 (1994).
[18] J. B. Elliott *et al.*, Phys. Lett. B **381**, 35 (1996).

[19] J. P. Bondorf *et al.*, Phys. Rep. **257**, 133 (1995).
[20] D. H. E. Gross, Rep. Prog. Phys. **53**, 605 (1990).
[21] B. K. Srivastava *et al.* (unpublished).
[22] G. F. Bertsch and S. Das Gupta, Phys. Rep. **160**, 189 (1988).
[23] Y. Yariv and Z. Fraenkel, Phys. Rev. C **24**, 488 (1981).
[24] J. Pochodzalla *et al.*, Phys. Rev. Lett. **75**, 1040 (1995).
[25] J. A. Hauger *et al.*, Phys. Rev. Lett. **77**, 235 (1996).
[26] P. G. Warren *et al.*, Phys. Rev. Lett. (submitted).
[27] G. Rai *et al.*, IEEE Trans. Nucl. Sci. **37**, 56 (1990); H. Wieman *et al.*, Nucl. Phys. **A525**, 617c (1991).
[28] G. Bauer *et al.*, Nucl. Instrum. Methods Phys. Res. A **386**, 249 (1997).
[29] D. L. Olson, The TAS application manual, 1992 (unpublished).
[30] M. L. Gilkes, Ph.D. thesis, Purdue University, 1994.
[31] M. L. Webb *et al.*, Phys. Rev. C **36**, 193 (1987).
[32] D. Cussol *et al.*, Nucl. Phys. **A561**, 298 (1993).
[33] K. Sümmerer *et al.*, Phys. Rev. C **42**, 2546 (1990).
[34] K. Nakai *et al.*, Phys. Lett. **121B**, 373 (1983).
[35] S. F. Butler and C. A. Pearson, Phys. Rev. **129**, 836 (1963).
[36] H. H. Gutbrod *et al.*, Phys. Rev. Lett. **37**, 667 (1976).
[37] M. L. Gilkes *et al.*, Phys. Rev. Lett. **75**, 768 (1995).
[38] R. Wada *et al.*, Phys. Rev. C **39**, 497 (1989).
[39] K. Hagel *et al.*, Nucl. Phys. **A486**, 429 (1988).
[40] P. Kreutz *et al.*, Nucl. Phys. **A556**, 672 (1993).
[41] T. Brohm and K. H. Schmidt, Nucl. Phys. **A569**, 821 (1994).
[42] J. B. Elliott *et al.*, Phys. Lett. B (in press).
[43] W. A. Friedman, Phys. Rev. C **42**, 667 (1990).
[44] S. Albergo *et al.*, Nuovo Cimento A **89**, 1 (1985).
[45] F. Ajzenberg-Selove, Nucl. Phys. **A490**, 1 (1988).
[46] X. Campi, H. Krivine, and E. Plagnol, Phys. Lett. B **385**, 1 (1996).
[47] A. Kolomiets *et al.*, Phys. Rev. C **54**, R472 (1996).
[48] M. B. Tsang *et al.*, Phys. Rev. C **53**, R1057 (1996).
[49] H. Xi *et al.*, Phys. Rev. C **54**, R2163 (1996).
[50] Z. Majka *et al.*, Phys. Rev. C **55**, 2991 (1997).
[51] F. Gulminelli and D. Durand, Nucl. Phys. **A615**, 117 (1997).
[52] S. Shlomo, J. N. De, and A. Kolomiets, Phys. Rev. C **55**, R2155 (1997).
[53] J. B. Natowitz *et al.*, Phys. Rev. C **52**, R2322 (1995).
[54] L. G. Moretto *et al.*, Phys. Rev. Lett. **76**, 2822 (1996).
[55] J. N. De *et al.*, Phys. Rev. C **55**, R1641 (1997).
[56] H. Jaqaman *et al.*, Phys. Rev. C **27**, 2782 (1983).
[57] G. Peilert *et al.*, Phys. Rev. C **39**, 1402 (1989).
[58] A. Das, R. Nayak, and L. Satpathy, J. Phys. G **18**, 869 (1992).
[59] V. Latora, M. Belkacem, and A. Bonasera, Phys. Rev. Lett. **73**, 1765 (1994); Phys. Rev. C **52**, 271 (1995).
[60] S. Pratt, C. Montoya, and F. Rouning, Phys. Lett. B **349**, 261 (1995).
[61] G. Papp and W. Nörenberg, Acta Phys. Hung. **1**, 241 (1995).
[62] J. P. Bondorf *et al.*, Nucl. Phys. **A443**, 321 (1985).
[63] H. W. Barz *et al.*, Nucl. Phys. **A531**, 453 (1991).
[64] R. T. deSouza *et al.*, Phys. Lett. B **300**, 29 (1993).
[65] S. C. Jeong *et al.*, Phys. Rev. Lett. **72**, 3468 (1994).
[66] W. C. Hsi *et al.*, Phys. Rev. Lett. **73**, 3367 (1994).
[67] M. A. Lisa *et al.*, Phys. Rev. Lett. **75**, 2662 (1995).
[68] P. G. Warren, Ph.D. thesis, Purdue University, 1996.
[69] E. Bauge *et al.*, Phys. Rev. Lett. **70**, 3705 (1993).
[70] D. Fox *et al.*, Phys. Rev. C **50**, 2424 (1994).